This is a preprint, the final version is subject to change, of the American Mineralogist (MSA)
Cite as Authors (Year) Title. American Mineralogist, in press.
DOI: https://doi.org/10.2138/am-2018-6229

Ni-serpentine nanoflakes in the garnierite ore from Campello Monti (Strona Valley, Italy): Népouite, but with some pecoraite outlines.

Gian Carlo Capitani

Dipartimento di Scienze dell'Ambiente e di Scienze della Terra, Università degli Studi di Milano-Bicocca, Italy.

Gennaro Ventruti

Dipartimento di Scienze della Terra e Geoambientali, Università di Bari, Italy.

Abstract

The garnierite ore at Campello Monti occurs as dark green colloform concretions covering surfaces, fractures, and filling veins in harzburgite rocks. The representative composition $(Ni_{2.45}Mg_{0.14}Cu_{0.12}Co_{0.05})_{\Sigma=2.76}Si_{2.10}O_5(OH)_4$ is consistent with a 7Å-phase, namely pecoraite or népouite. Relevant chemical features are an exceptionally high Ni/Mg ratio, a significant level of Cu substituting for Ni, and a low content of S, possibly in tetrahedral sites.

Olivine and orthopyroxene in the harzburgite host rock are only partially serpentinized, do not contain detectable Ni, and are almost iron free. The green coating probably originated from ground-water solutions that leached nearby weathered peridotites and sulfide ores, and deposited less-mobile elements along fractures and voids of the host peridotite, just outside their provenance area.

Bulk techniques, such as X-ray powder diffraction and infrared spectroscopy, do not confidently distinguish between népouite and pecoraite, although the comparison with synthetic, implicitly pure polymorphs indicates népouite as the best matching phase. On the other hand, HRTEM clearly

Always consult and cite the final, published document. See http:/www.minsocam.org or GeoscienceWorld

shows that garnierite is mostly constituted by plumose aggregates made of curved crystals with frayed tips, a few nanometers thick along the stacks and a few tens of nanometers long (nanoflakes). All known lizardite stacking sequences, namely 1*T*, 2H_1, and 2H_2, have been locally observed, even though most crystals show stacking disorder.

The recorded nanostructure suggests possible explanations for the recurrent anomalies (low oxide totals, high ^{IV}T/^{VI}M cation ratios, etc.) found in EMP analyses of garnierites. The small grain size, the high density of defects, and the structural arrangement actually intermediate between lizardite and chrysotile probably explain the ambiguities that occurred during the characterization with bulk techniques.

The results obtained in this study may have important implications in technological applications involving Ni-phyllosilicates, and in the development of new hydrometallurgical ore processing methods.

Key words: garnierite; népouite; nanoparticles; transmission electron microscopy.

Introduction

Serpentinites originate from the hydrothermal alteration of ultramafic rocks. They are abundant at mid-ocean ridges, where the oceanic crust forms and almost contemporarily may experience retrograde metamorphism (e.g., Mével 2003), and at subduction zones, where two plates of oceanic lithosphere, mostly ultrabasic in composition, converge and where a large amount of fluids circulate along transform faults and “outer rise” fractures (Kerrick 2002). As a corollary, considerable outcrops of serpentinites occur along orogenic belts, sampled from the down-going slab and exhumed by tectonics after the included basin is completely recycled.

Always consult and cite the final, published document. See http:/www.minsocam.org or GeoscienceWorld

Serpentine minerals are hydrous magnesium silicates with the ideal formula $Mg_3Si_2O_5(OH)_4$, which occur in nature in four principal polymorphs, distinguished by the shape of the building *TO* layer. Lizardite is the serpentine mineral that forms flat layers. Different polytypes with different stacking of the *TO*-layers have been reported so far (e.g., Mellini and Zanazzi 1987; Brigatti et al. 1997). Chrysotile adopts a cylindrical structural arrangement in which the tetrahedral sheet occupies the internal position, and is the main constituent of asbestos (e.g., Cavallo and Rimoldi 2013 and references therein). Antigorite is based on a wave-like structure in which the tetrahedral sheet periodically inverts polarity (Capitani and Mellini 2004). Different antigorite structures (polysomes) are possible depending on the wavelength (Capitani and Mellini 2006, 2007). A rarer polymorph is polygonal serpentine, which forms fibers with a polygonal cross section, made up of flat layers in sectors. The number of sectors is always either 15 or 30, with curved connections between them (Mugnaioli et al. 2007).

Ni-serpentines are much less abundant in nature. The Ni analogue of chrysotile is pecoraite (Faust et al. 1969), whereas the Ni analogue of lizardite is népouite (Brindley and Maksimović 1974). Ni-analogues for antigorite and polygonal serpentine have not been reported so far. Ni-serpentines are important ore minerals for Ni (e.g., Butt and Cluzel 2013; Villanova-de-Benavent et al. 2014). Nickel is extracted from two principal types of ore deposits: i) sulfide ores, normally developed by a magmatic concentration process, and ii) laterite ores, supergene deposits formed by the pervasive chemical and mechanical weathering of the parent rock, commonly peridotite. Laterite ores are further distinguished in: i) oxide deposits, where Ni is mostly associated with goethite in the uppermost part of the soil profile, and ii) hydrous silicate deposits, where Ni is hosted in garnierite within the saprolite (Brand et al. 1988; Ridley 2013). Garnierite is the general name used to define greenish, poorly crystallized, clay-like Ni ore that generally comprises an intimate mixture of Ni/Mg hydrosilicates like serpentine, talc, sepiolite, smectite, and chlorite (Brindley and Hang 1973; Springer 1974).

Always consult and cite the final, published document. See http:/www.minsocam.org or GeoscienceWorld

The formation of garnierite may either result from the direct clay-like alteration of olivine-rich rocks, generally leading to low Ni/Mg ratio garnierite minerals, or from the weathering and leaching of Ni under supergene conditions of the altered peridotite and subsequent re-precipitation of Ni-serpentine (Pecora et al. 1949). In the classical *per descensum* model (e.g., Brand et al. 1998; Butt and Cluzel 2013; Villanova-de-Benavent 2014), the formation of garnierite ore is related to the development of a thick lateritic profile above a faulted and altered ultramafic host rock, under tropical climate conditions. In this model, the Ni leaches out from the oxide ore in the upper laterite (which is richer in Ni than the unweathered host rock), and is accumulated downward in fractures of the underlying saprolite, within the structure of early-formed and newly-formed 1:1- and 2:1-layer silicates. Recently, Fritsch et al. (2016) proposed an alternative model to explain the formation of garnierite ore in New Caledonia. According to this model, the formation of hydrous Mg/Ni silicate ore can be schematized by a two-step alteration process. The first step would result in the formation of hydrous Mg/Ni silicates after alteration of the serpentine veins in serpentinized peridotite through tectonically reactivated faults. The second step would correspond to the lateritization of the intensely fractured and mineralized zones of the peridotites. Unlike the *per descensum* model, in the latter model it would be the hydrous Mg/Ni layer silicates of the thick serpentine veins that ‘‘feed’’ Ni into the oxide ores in the laterite horizon, and not the reverse.

Nickel usage has increased over time in parallel with economic development. According to the International Nickel Study Group[1], the world’s primary nickel production recorded an annual growth rate of 5.5% in the period from 2011 to 2015. Nickel-rich laterite deposits account for about 40% of the world’s Ni production, but due to the ongoing depletion of sulfide ores, an increase in the Ni production from laterite deposits is expected in the future (Kesler and Simon 2015). Although the metallurgical extraction of Ni from silicate and oxide minerals requires significantly greater energy than extraction from Ni-bearing sulfide minerals (Ridley 2013), the development of

[1]International Nickel Study Group, (Nickel) Production, uses and prices, URL:http://www.insg.org/prodnickel.aspx. Accessed: 2017-12-04. (Archived by WebCite® at http://www.webcitation.org/6vSO1g4Rx)

Always consult and cite the final, published document. See http:/www.minsocam.org or GeoscienceWorld

new hydrometallurgical ore processing methods, including high pressure acid leaching (HPAL) and atmospheric (acid) leaching (AL), makes the processing of laterite ores economically more feasible than in the past (McDonald and Whittington 2008). In this respect, the hydrous silicate deposits are of special interest, since they show the highest Ni grades among the laterite ores, ranging from 1.8 to 2.5 wt. %, and the Ni content of the garnierites can be as high as 40 wt. % (Soler et al. 2008). However, despite the importance of garnierites as Ni ore, significant uncertainties regarding the composition, structure, and nanostructure of these ill-defined phases still remain.

In this study, a garnierite ore associated with ultramafic rocks from the Strona Valley (Western Alps, Italy) is reported for the first time, with the aim of contributing to a deeper knowledge of the garnierite minerals in general. The detailed characterization, down to the near-atomic scale, allows the understanding of some common structural and compositional anomalies of garnierite minerals, and the envisaging of a positive response to acidic leaching for Ni extraction of the investigated ore, and of similar ore deposits all around the world.

Geological Context

The studied samples are from Campello Monti, Strona Valley, Western Alps, Novara, Italy (Fig. 1). The area has been mined for Ni-sulfides with numerous interruptions from 1865 to 1949, after which the mining activity definitely ceased. The reasons that determined the cessation of the mining activities are both logistic and geological. The altitude, 1300–1600 m a.s.l., and the acclivity of the area made the mining yard operations, and even the installation of the related infrastructure, difficult. The lack of a mineralized dyke system, the hardness of the host rock, and the low concentration of the ore mineral (2%), made the cost of the extracted Ni not competitive with that coming from New Caledonia and Canada (Zanoletti 2007).

The mineralized rocks at Campello Monti are peridotites and olivinic pyroxenites of the “diorito-kinzigitic” complex of the Ivrea Verbano Zone. This is a unit of the crystalline basement of the

Always consult and cite the final, published document. See http:/www.minsocam.org or GeoscienceWorld

Southern Alps, of Paleozoic age, formed by pelitic and semipelitic metasediments, subordinated marbles and amphibolites, and mafic and ultramafic, highly metamorphosed, rocks (Boriani and Sacchi 1973). The mineralized bodies have lenticular or irregular shapes, sometimes showing stratiform arrangements. The metallic paragenesis is constituted by pyrrhotite, chalcopyrite, and pentlandite, the latter sometimes transformed into bravoite. The metallic minerals are minutely disseminated within the ultramafic rocks or concentrated in small veins or lenses (Zucchetti 1979). The alteration of these ultramafic rocks, which are locally serpentinized and talcized, and of the associated sulfides, probably provided the Ni necessary for the formation of the garnierite ore that is the object of this study.

Experimental Methods

Several hand specimens from Campello Monti, all similar in macroscopic appearance, were considered for this study. Both the green botryoidal coating constituting the garnierite ore and its host rock were investigated.

Two representative specimens of the host rock were investigated by means of optical microscopy, electron microscopy (SEM), X-ray powder diffraction (XRPD), and energy dispersive X-ray fluorescence (EDXRF) at the Department of Earth and Environmental Sciences of the University of Milano-Bicocca. Petrographic investigations were carried out on standard (2.80 x 4.60 x 0.03 mm) polished thin sections of the host rock cross-cutting the green coating. SEM observations and energy dispersive (EDS) analyses were performed with a Tescan VEGA TS 5136XM with a tungsten filament and equipped with an EDAX GENESIS 4000XMS EDS system. Operating conditions were 20 keV and 190 pA, for a probe size at the sample surface of ~50 nm (see Fig. 3.8 in Reed 2005). Under these conditions, in a typical ultramafic mineral such as forsterite, Monte Carlo simulations of the electron/sample interaction sphere indicate a spatial resolution of the probe of ~4 μm. The standardless method and the ZAF correction method were used for semi-quantitative

Always consult and cite the final, published document. See http:/www.minsocam.org or GeoscienceWorld

146 analyses. The chemical formulae of olivine, pyroxene, amphibole, spinel, chlorite, carbonates,
147 serpentine, and talc were recalculated on the basis of 8, 12, 46, 8, 28, 4, 14, and 22 negative
148 charges, respectively.

149 Chemical analyses of the host rock were obtained with a PANalytical Epsilon 3^X EDXRF
150 instrument. Five grams of rock powdered in an agate mortar were mixed with five grams of
151 hydrogen borate and pressed at 15 tons for one minute. Anorthosite, basalt, diorite, and norite of
152 known compositions were used as standards for quantitative analyses. Volatile components (H_2O
153 plus CO_2) were determined through the weight loss on ignition (LOI). The Fe^{3+}/Fe^{2+} ratio was
154 determined through $KMnO_4$ redox titration.

155 For XRPD analyses, the samples were ground in an agate mortar, back-loaded in aluminum holders,
156 and analyzed with a PANalytical X'Pert-Pro PW3060 diffractometer, operating in Bragg-Brentano
157 specular (θ-θ) geometry and equipped with an X'Celerator position-sensitive detector.
158 Diffractometer scans were recorded at 40 mA and 40 kV (CuK_α radiation) in the 5–90° 2θ range,
159 with a step size of 0.017° and counting time of 0.40 s per step. A Ni filter along the diffracted beam
160 path was used to filter out the CuK_β radiation. The sample holder was allowed to spin horizontally
161 during measurements to improve particle statistics. The identification of major and minor phases
162 was done using the X'Pert High Score software (PANalytical) using the ICSD PDF2-2004
163 database. Quantitative phase analyses (QPA) were performed with the Rietveld method (Hill 1991;
164 Bish and Post 1993) implemented in the GSAS/EXPEGUI (Larson and Von Dreele 2004).

165 The garnierite constituting the green botryoidal coating of the samples was investigated by wave
166 dispersive (WDS) electron microprobe (EMP) analyses, X-ray powder diffraction (XRPD), Fourier
167 transform infrared spectroscopy (FTIR), and transmission electron microscopy (TEM). For WDS-
168 EMP chemical analyses, some fragments of the green coating were embedded in epoxy resin and
169 polished. EMP data were collected at the Institute of Geosciences and Earth Resources (IGC-CNR)
170 in Florence using a Jeol JXA 8600 instrument with a W filament, operating at 15 kV and 10 nA.

Always consult and cite the final, published document. See http:/www.minsocam.org or GeoscienceWorld

Under these conditions, the beam size at the sample surface is ~250 nm (see Fig. 3.8 in Reed 2005). Monte Carlo simulations of the electron/sample interaction sphere indicate a spatial resolution of ~3 μm for népouite. Counting times of 15 s for peak and 5 s for background were used for Si, Al, Fe, Ni, and Mg, whereas 40 s for peak and 20 s for background were used for S, Co, Cu, and Mn. Raw data were corrected using the PAP matrix correction (Pichou and Pichoir 1991) method and quantified using the following standards: albite (Si), olivine (Mg), plagioclase (Al), bustamite (Mn), ilmenite (Fe), celestine (S), cuprite (Cu), metallic Co and Ni (for Co and Ni, respectively). For these elements, the detection limit is estimated to be between 0.04 and 0.07 wt. %, and the relative error is below 13.8% for oxide concentrations above 0.5 wt. %, below 8.8% for oxide concentrations above 1.0 wt. %, and below 3.1% for oxide concentrations above 5%.

For XRPD, fragments of the coating were detached with a scalpel from the hand specimen surface and coarsely ground in the agate mortar. Any possible contaminant discernible under the stereo-microscope at this stage was removed with the aid of a magnet and a needle. The enriched powder was further ground for powder X-ray analyses and loaded into a 0.3 mm glass capillary.

Powder diffraction patterns were collected at the University of Bari with a PANalytical Empyrean diffractometer equipped with a real-time multiple strip (RTMS) PIXcel3D detector and a focusing X-ray multilayer mirror. The X-ray tube (CuK_α radiation) was operated at 40 kV and 40 mA, and diffraction data were collected in the 5–85° 2θ-range. In order to minimize preferred orientation, the capillary was allowed to rotate during acquisition, and to improve the signal-to-noise ratio, intensity data were averaged over three individual scans collected in continuous mode, with a step size of 0.013° 2θ and a counting time of 1.40 s per step.

FTIR measurements were acquired at the University of Bari using a Nicolet 380 FTIR spectrometer equipped with an EverGlo source, a KBr beamsplitter, and a deuterated triglycine sulfate (DTGS) detector. FTIR spectra were collected in transmission mode on pellets of approximately 2 mg of the same powder used for XRPD diluted in 200 mg of KBr. The pellet was also dried at 110°C for at

Always consult and cite the final, published document. See http:/www.minsocam.org or GeoscienceWorld

196 least 12 hrs. to remove possible adsorbed water. The nominal resolution was set to 4 cm^{-1}; 128
197 scans over the range 400–4000 cm^{-1} were averaged for both sample and background.

198 For TEM investigations, two different sample preparation methods were used. In one case, the same
199 powder used for XRPD analyses was dispersed in ethanol and ultrasonicated, then a 5 μl drop of the
200 suspension was deposited on carbon-coated Au-grids. These grids were mainly used for TEM-EDS
201 chemical analyses. Two additional samples were prepared from the largest fragments detached from
202 the green coating. These samples were embedded in epoxy resin, mechanically milled down to 30
203 μm with silicon carbide, double polished with alumina, fixed on a Cu ring, and gently ion-milled
204 down to electron transparency. Ion milling was carried out at the Geology Department "Ardito
205 Desio" of the University of Milan with a Gatan precision ion polishing system (PIPS). Before TEM
206 observations, these samples were carbon coated to avoid electrostatic charging within the TEM.

207 TEM observations were performed at the Department of Physical Sciences, Earth, and Environment
208 of the University of Siena with a Jeol JEM 2010 operating at 200 keV and equipped with an Oxford
209 Link energy dispersive spectrometer for X-ray microanalysis (EDS), and with an Olympus Tengra
210 2.3k x 2.3k x 14-bit slow scan CCD camera for image acquisition. To remove noise contrast due to
211 amorphous materials, high resolution (HR) TEM images were rotationally filtered (Kilaas 1998)
212 with the HRTEM filter (Mitchell 2007), as implemented in the Gatan Digital Micrograph version
213 3.9. In some cases, HR images were further filtered, applying proper masks on the fast Fourier
214 transforms (FFT) of the image to retain the periodic signal only, and then computing the inverse
215 Fourier transform (IFT). High resolution image simulations were performed with JEMS ©, a Java
216 version Electron Microscopy Software, by P. Stadelmann (CIME-EPFL, Switzerland).

217 Finally, semi-quantitative EDS analyses were obtained with the standardless method and corrected
218 for absorption following Van Cappellen and Doukhan (1994).

219

Always consult and cite the final, published document. See http:/www.minsocam.org or GeoscienceWorld

Results

Petrography and mineral chemistry of the host rock

The garnierite collected for this study has the appearance of a thin, green coating over a dark brown, locally reddish, massive rock (Fig. 2). Under the optical microscope, the latter consists of olivine, orthopyroxene, and opaque minerals forming a coarse granular texture (Fig. 3a and b). Opaque minerals are mostly spinel with a corona texture of chlorite (Fig. 3c and d) and sulfides. Olivine and orthopyroxene may be partially altered to serpentine and talc, respectively. The alteration attacks mineral joints and rims, leaving the characteristic magnetite strings (Fig. 3e and f). Alteration products also seal veins cross-cutting the rock.

The chemical composition of the two host rock samples obtained by EDXRF in this study are comparable with that obtained by wet chemical analysis by Bertolani (1968) for unserpentinized peridotite from the same area (Table 1). All samples show low NiO content and quite different volatile content. Surprisingly, sample N2, with the lower LOI value, is also the most altered under the optical microscope, i.e. richer in hydrous phases. This apparent inconsistency can be at least in part explained by the higher FeO content: the weight loss due to the volatile component may be partially compensated by the oxidation of iron, which entails an increase in mass. Alternatively, this difference may just reflect the larger accidental uptake of vein material in one sample than in the other. Finally, the slightly different SiO_2/MgO ratio may suggest different olivine/orthopyroxene proportions in the studied samples, consistent with the observations from the thin sections.

Average compositions obtained by semi-quantitative EDS analyses on polished thin sections for forsterite and enstatite read ($Mg_{1.67}Fe_{0.33}SiO_4$) and $[(Ca_{0.01}Mg_{1.66}Fe_{0.29}Al_{0.04})_{\Sigma=2}(Al_{0.04}Si_{1.96})_{\Sigma=2}O_6]$, respectively. Minor diopside and pargasitic hornblende detected by SEM-EDS show average compositions of $[(Ca_{0.89}Mg_{0.92}Fe_{0.09}Al_{0.07})_{\Sigma=1.97}(Si_{1.98}Al_{0.02})_{\Sigma=2}O_6]$ and $[(Na_{0.72}K_{0.12})_{\Sigma=0.84}Ca_{1.77}(Mg_{3.60}Fe_{0.65}Al_{0.59}\ Ti_{0.19}Cr_{0.09})_{\Sigma=5.13}(Si_{6.30}Al_{1.70})_{\Sigma=8}O_{22}(OH)_2]$, respectively. The opaque minerals are mostly a Cr-rich spinel with average composition of

Always consult and cite the final, published document. See http:/www.minsocam.org or GeoscienceWorld

245 $[(Mg_{0.51}Fe_{0.49}Zn_{0.01})_{\Sigma=1.01}(Al_{1.49}Cr_{0.42}Fe_{0.12})_{\Sigma=2.03}O_4]$, altered at the borders to Cr-rich magnetite
246 $[(Fe_{0.99}Mg_{0.03})_{\Sigma=1.02}(Fe_{1.30}Cr_{0.71}Al_{0.10})_{\Sigma=2.11}O_4]$. The reaction rim bordering spinel is clinochlore
247 $[(Mg_{4.76}Fe_{0.27})_{\Sigma=5.03}Al_{0.93}(Si_{3.14}Al_{0.86})_{\Sigma=4}O_{10}(OH)_8]$, and serpentine and talc altering olivine and
248 orthopyroxene along joints and rims yield average compositions of
249 $[(Mg_{2.74}Fe_{0.13})_{\Sigma=2.87}Si_{2.06}O_5(OH)_4]$ and $[(Mg_{2.99}Fe_{0.15})_{\Sigma=3.14}(Si_{3.83}Al_{0.13})_{\Sigma=3.96}O_{10}(OH)_2]$, respectively.
250 The magnetite associated with serpentine and talc is almost pure, and thus distinguished from the
251 former spinels. A few veinlets of dolomite $[(Mg_{1.01}Ca_{0.96}Fe_{0.06})_{2.03}(CO_3)_2]$ were detected by SEM-
252 EDS, which was also observed to be finely intermixed with serpentine. Finally, the scarce and
253 corroded sulfides yield approximate compositions FeS, $CuFeS_2$, and $FeNiS_2$, consistent with
254 pyrrhotite, chalcopyrite, and pentlandite, respectively (Fig. 3g).

255 On the basis of Rietveld refinements performed on X-ray diffractograms of two representative
256 samples, the major mineral constituents of the host rock are: olivine (68–42%), orthopyroxene (28–
257 36%), talc (2–9%), serpentine (1–5%), spinel (1–3%), and hornblende (0–5%). These data plot in
258 the harzburgite field at the boundary with the olivine-pyroxenite field, both described in this area
259 (Bertolani 1968).

260

261 Chemical composition and microstructure of garnierite

262 Under the optical microscope, garnierite consists of green, banded, botryoidal aggregates and shows
263 first-order birefringence in crossed polars, with undulose, parallel extinction. The crossed polars
264 appearance is consistent with parallel growth of fibers, or minute radiating crystals, elongated
265 perpendicularly to the bands (Fig. 4a and b). The green coating is restricted to the sample surface
266 and along fractures penetrating the host rock, and may envelope rounded saprolite fragments,
267 mainly iron oxides and hydroxides, and altered olivine (Fig. 4c and d).

Always consult and cite the final, published document. See http:/www.minsocam.org or GeoscienceWorld

In backscattered electron (BSE) images, the green coating shows a colloform texture with concentric zoning. Three main zones can be identified: 1) an inner zone characterized by small coalescent spheroids with many voids and interstices; 2) a massive intermediate zone with smooth concentric zoning; 3) an outer rim with fine-scale zoning and relatively dark bands. The apparent thickness of these zones varies within the same sample and also depends on the cut of the sample, but is on the order of 100 microns for the inner and intermediate zones and is relatively thin, on the order of tens of microns, for the outer zone (Fig. 5a and b). As expected, the whole texture is a consequence of the chemical zoning (Fig. 5c and d).

It turns out that most point analyses, calculated on the basis of seven oxygens, show compositions consistent with népouite and pecoraite, apart from a few spot analyses from the outer zone, with marked higher Cu and Al contents, which will be considered later. In Table 2, average WDS microprobe compositions of the intermediate zone of three different mounts prepared from the same hand specimen are reported. The most notable feature is the variability in Ni and Mg, which are clearly anti-correlated (Fig. 6a), as well as Ni and Cu (Fig. 6b), suggesting isomorphous substitution of Mg and Cu for Ni in the octahedral site. The darker bands normally show a lower Ni/Mg ratio. In addition to Si, Ni, Mg, and Cu, other cations like Co, Mn, and S are detected at significant levels, whereas Fe and Al are always very low or not detected at all. Higher Co and Mn contents seem present in the brighter bands, while S and Cu do not show any clear preference. Co and Mn, which reasonably should occupy the octahedral site, do not show any clear correlation, probably because of their low concentration which makes the analytical datum inaccurate and the plot unclear.

A significant excess of tetrahedral cations and deficiency of octahedral cations are recorded in these analyses, like in many other reports (e.g., Song et al. 1995; Brindley and Hang 1973; Brindley and Wan 1975; Wells et al. 2009; Villanova-de-Benavent et al. 2014). In this case, however, it should be noted that S also contributes to the tetrahedral cation summation since it has been considered as S^{6+} in the calculation and attributed to the tetrahedral sites, according to the faint but significant

Always consult and cite the final, published document. See http:/www.minsocam.org or GeoscienceWorld

anticorrelation with Si (Fig. 6c). The averages of oxides summation (Table 2) span between ~85.3 and ~92.5 wt. %, which are, albeit slightly, lower and higher than expected for ideal lizardite (87.0 wt. %) and ideal népouite (90.5 wt. %), respectively. These values are comparable with those of many other descriptions of garnierites (e.g., Faust 1966; Brindley and Hang 1973; Springer 1974; Song et al. 1995; Villanova-de-Benavent et al. 2014). Finally, the measured compositions, when plotted in the ternary Si-Mg-Ni system (Fig. 6d), cluster close to the népouite field and show a tail towards "Ni-karpinskite", an intermediate phase between serpentine-like and talc like-phases — not accepted as mineral species by IMA — with composition $(Ni,Mg)_2Si_2O_5(OH)_2$. If real, i.e not due to analytical artifacts such as an interplay of uncounted cations, this trend could indicate either an increase of octahedral cation vacancies in the Ni-serpentine, or intermixing with 2:1 layer structures, with decreasing of the Ni/Mg ratio.

The outer zone is characterized by a general increase of the Mg, Al, and Cu contents, and by a decrease of Si and Ni. Al is clearly anticorrelated with Si, and Cu with Ni. It should be noted that the Cu peak and the Al peak are out of phase. A possible explanation is that Cu and Al belong to two different phases with different abundaces in the banded outer zones (Fig. 5c and d). Finally, an increase of S is also recorded in the outer zone, which seems correlated with Al.

In Table 3 some selected spot analyses from the outer zone, characterized by the highest contents of Mg, or Al, or Cu are reported. It is worth noting that the outer zone is characterized by a fine-scale zoning, which is finer than the sample volume excited by the microprobe, thus the composition of each individual band is difficult to obtain. Moreover, it cannot be excluded that more than one single phase could be present in such bands. As a consequence, most analyses cannot be straightforwardly recalculated on the basis of known phases — although, for the sake of comparison, the same base of seven oxygens as for Ni-serpentine is maintained — with the exception of some spot analyses, which can be still attributed to Ni-serpentine, even if they are richer in Mg than the Ni-serpentine detected in the intermediate zone (cfr. Table 3 with Table 2).

Always consult and cite the final, published document. See http:/www.minsocam.org or GeoscienceWorld

Finally, a few spot analyses from the inner zone can be attributed to Ni-serpentine, analogous to that present in the intermediate zone (cfr. Table 3 with Table 2).

Crystallography of the Ni-serpentine

The XRPD pattern of garnierite from Campello Monti shows six relatively sharp peaks and three broader peaks at 42.25, 53.35, and 71.73° 2θ, which look like shoulders or smooth bulges rather than real peaks, suggesting that the sample lacks a perfect long-range order, and/or it is very fine grained (Fig. 7). Probably because of the poor crystallinity, mineral identification is ambiguous. In fact, as evidenced in Figure 7, where the pattern of the Ni-serpentine from Campello Monti is compared with those of pecoraite and népouite from Kwangcheon, Korea (Song et al. 1995), the main difference between pecoraite and népouite is that the chrysotile-type mineral has only one strong peak at 1.53 Å (60.5° 2θ), while the lizardite-type mineral has two distinct lines at 1.53 and 1.50 Å (Milton et al. 1983; Song et al. 1995). The Ni-serpentine from Campello Monti actually shows only one single peak at 1.53 Å, although a shoulder on the right side suggests that it could be convoluted with the peak at 1.50 Å.

The powder diffraction data of the garnierite from Campello Monti are shown in Table 4 and compared with those of pecoraite and népouite. It should be noted that the first peak (at ~7.60 Å), tied to the *c*-axis length and thus to the interlayer spacing, occurs at a significantly lower 2θ position than expected according to the pecoraite and népouite structures. This deviation (quantifiable in ~0.24 Å) is probably an artifact that arises from the high background occurring at low 2θ. However, the possibility of a slightly expanded cell should not be completely discarded, since, as can be inferred from the peak profile of the current diffractogram, the crystallite size of the investigated material is very small, i.e. in the nanoparticle range, and it is well known that

Always consult and cite the final, published document. See http:/www.minsocam.org or GeoscienceWorld

nanoparticles show slightly expanded cells with respect to the corresponding bulk specimen (e.g., Reynolds 1968; Zhang et al. 2002).

The unit cell refinement starting from the pecoraite $2M_{c1}$ parameters leads to the following unit cell parameters: a = 5.27(2), b = 9.18(1), c = 14.76(3) Å, β = 92.16°. Refinement in the *P*31*m* népouite 1*T* structure gives comparatively worse results (compare *RMs* deviations in Table 4) and the following cell parameters: a = 5.28(1), c = 7.36(2) Å. This result, however, should be treated with caution since the small number of reflections and their flat profile make the refinement very prone to errors.

The same powder analyzed with XRPD was also analyzed by FTIR. The resulting spectrum is plotted in Figure 8 along with reference spectra of natural népouite and pecoraite from the literature, and the vibrational frequencies of the observed bands are shown in Table 5. FTIR data for the garnierite of Campello Monti appear to agree better with the literature data for synthetic népouite than for synthetic pecoraite or natural pecoraite and népouite. In particular, the inner surface O-H stretching bands at 3646 and 3610 cm^{-1} (Balan et al. 2002) and the Ni-OH libration band at 673 cm^{-1} (Farmer 1974) are discriminant in this comparison.

Nanostructure of the Ni-serpentine

TEM observations were focused in the wide intermediate zone, where microprobe analyses indicate Ni-serpentine with a slightly varying Ni/Mg ratio. The average composition from 11 TEM-EDS spot analyses randomly taken on the investigated areas, expressed on the basis of 14 positive charges, reads: $(Ni_{2.11}Mg_{0.15}Co_{0.07}Cu_{0.31})_{\Sigma=2.64}Si_{2.17}O_5(OH)_2$, which is consistent, within the experimental error, with the microprobe analyses.

A bright field (BF) image and a lattice fringe image from an ion-milled sample of the Ni-serpentine are shown in Figures 9a and 9b, respectively. These images clearly show that the Ni-serpentine

Always consult and cite the final, published document. See http:/www.minsocam.org or GeoscienceWorld

forms plumose aggregates of crumpled particles no longer than a few tens of nanometers and no thicker than a few nanometers. Particles have flat structure (nanoflakes) like lizardite and népouite, though bent and frayed, and not a cylindrical shape like chrysotile and pecoraite. The interplanar distance measured on HR images is about 7.3 Å, consistent with one-layer serpentine.

A selected area electron diffraction (SAED) pattern taken on the plumose aggregate of Figure 9a is shown in Figure 9c, along with the related radial profile (Fig. 9d). The SAED pattern contains a few continuous and diffuse rings typical of randomly-oriented nanoparticles, and is entirely consistent, within the experimental error, with the XRPD pattern, although less resolved and with a much higher background. With reference to the refined XRPD pattern, the (110) and the (003) peaks are convoluted into one large peak at 2.57 Å (Fig. 9d); the (002) peak at 3.61 Å is present as a large shoulder on the flank of the (010) peak (4.54 Å); the (001) peak at 7.43 Å is almost completely hidden by the huge background around the transmitted beam (towards the center of the diffractogram); the diagnostic (300) peak occurs at 1.56 instead of 1.53 Å. Other detected peaks are: a shoulder on the right side of the (003) peak at 2.18 Å; a small, flat peak at 1.75 Å; and a relatively sharp peak at 1.35 Å. These peaks were also detected in the X-ray powder diffractogram, although at a slightly higher angle, and indexed after refinement as (112), (210), and (220), respectively. Other high-angle diffuse rings (at 1.01 and 0.91 Å) could not be indexed with certainty because of the many closely-spaced reflections potentially occurring at higher Bragg angles.

TO stacking sequence and disorder

To decipher the stacking of népouite, as for any sheet-silicate, two-dimensional HR images are required. In most cases, observations of the same area along two non-equivalent directions perpendicular to the stacking direction are required (e.g., Kogure 2002; Fregola et al. 2009; Capitani et al. 2016). However, because of the quick amorphization of beam-sensitive phyllosilicates, often

Always consult and cite the final, published document. See http:/www.minsocam.org or GeoscienceWorld

one-dimensional lattice fringe images only are obtained, as shown in Figure 5b, which are not enough to distinguish different polytypes.

In the present investigation, two-dimensional information was obtained by making use of low-dose operation and improving the image quality through Fourier filtering. To help interpret the two-dimensional HR experimental images, the HR image simulation of népouite was used. For this purpose, the crystal structures of the three different known polytypes of lizardite, 1*T* (Mellini 1982), $2H_1$ (Mellini and Zanazzi 1987), and $2H_2$ (Brigatti et al. 1997) were taken and modified by substitution of the octahedral cations (Mg and Fe) by Ni. It turns out that with the current instrumental conditions only the ⟨110⟩ directions allow a two-dimensional view of the structure, and thus the possibility of simulating the stacking sequence. All the other directions, namely ⟨120⟩, rotated 30° apart around the *c*-axis, require higher resolution to distinguish structural features within the layer and thus lead to (001) lattice fringe only. ⟨110⟩ HR images for the three polytypes were then simulated for defocus values between the optimal Scherzer (35 nm) and the extended Scherzer (42.5 nm), and for thicknesses between 2 and 10 nm. The results are shown in Figure 10, for a sample thickness of 4 nm and a defocus of 42.5 nm. It should be noted that népouite 1*T* and $2H_1$ cannot be distinguished in this projection, since they show analogous contrast with the same "straight" sequence. They would be distinguished in ⟨120⟩ projections if higher resolution were possible, since along that projection népouite 1*T* shows a straight sequence, whereas népouite $2H_1$ shows a "zig-zag" sequence. On the other hand, népouite 1*T* and $2H_1$ can be distinguished from népouite $2H_2$ on ⟨110⟩ HR images, since the latter shows a "zig-zag" sequence.

The results show that népouite nanoflakes possess both ordered straight sequences, as in lizardite 1*T* and $2H_1$ (Fig. 11a), and ordered zig-zag sequences, as in the lizardite $2H_2$ polymorph (Fig. 11d), although ordered stacking sequences involve crystal thickness of just a few unit cells. Moreover, most crystals show disordered sequences and dislocation-like defects (Fig. 11b and 12). These

Always consult and cite the final, published document. See http:/www.minsocam.org or GeoscienceWorld

observations make the concept of "long range order" quite feeble for this mineral, confirming the first impression given by XRPD and SAED.

Discussion and Conclusions

Crystal chemistry of népouite

Garnierite from Campello Monti, at least with regard to the widespread dark green colloform concretions found in peridotite fractures and veins, is constituted mostly by népouite, with the following chemical features: i) high Ni content, which is anti-correlated with Mg; ii) significant amounts of Cu, apparently substituting for Ni (and Mg); iii) excess of tetrahedral cations and deficiency of the octahedral ones; iv) highly variable oxide totals often lower than expected; v) presence of S, possibly in the tetrahedral position.

The Ni-serpentine described in this paper is among the richest in Ni (2.074–2.570 a.p.f.u.) ever reported in the literature (compare Fig. 6d with Fig. 12d of Villanova-de-Benavent et al. 2014), and contains significant amounts of Cu (0.060–0.150 a.p.f.u.), which is apparently in solid solution with Ni and Mg in the octahedral site. The high Ni and Cu contents probably derive from efficient leaching of these elements in the parent peridotite, present either as minor elements in olivine or in Ni-Cu sulfides.

The anti-correlation of Ni and Mg reaffirms the solid solution between népouite and lizardite (Brindley and Hang 1973; Brindley and Wan 1975; Baron and Petit 2016). In the studied Ni-serpentine, however, the entry of Mg in the octahedral site is accompanied by a shift towards more silicic, talc-like compositions. This trend has already been observed (e.g., Suárez et al. 2011), but apparently contradicts reports on garnierites from other localities where 7-Å and 10-Å phases coexist in the same sample, and the 10-Å phase is always richer in Ni than the 7-Å one (Esson and Carlos 1978; Poncelet et al. 1979; Soler et al. 2008; Villanova-de-Benavent et al. 2016).

Always consult and cite the final, published document. See http:/www.minsocam.org or GeoscienceWorld

Slow scan diffractograms taken in the 3–30° 2θ region on oriented samples do not show any additional peak relating to any 10-Å phase, and XRPD patterns recorded after ethylene glycol treatment do not show any significant shift of the (001) peak (supplementary material S1), whose occurrence, according to Choulet et al. (2016), would indicate the presence of interstratified serpentine-like and smectite-like phases. Accordingly, lattice fringes with periodicity other than 7-Å were not observed in the studied samples at the TEM, either as a single phase or as intergrowths in népouite. A possible explanation of the observed shift towards more silicic compositions is that the Mg for Ni substitution is accompanied by an increase in octahedral vacancies.

According to previous interpretations (Brindley and Hang 1973; Brindley 1980), the excess of tetrahedral cations coupled with the deficiency of octahedral ones in microprobe analyses are related to: i) the presence of colloidal silica within the analyzed volume; ii) intergrowths of silica-richer phases; iii) leaching of octahedral cations at the edges of the clay particles. In the present study, the most plausible mechanism seems to be the latter, which would remove the soluble M^{2+} cations and OH^- from the edges, leaving a silica residue (Brindley 1980; Suárez et al. 2011). The curved crystals with frayed tips observed at the TEM actually suggest altered crystal chemistry at the border of the crystals. Given the very small grain size and the consequent high surface/volume ratio, it is very probable that such altered crystal chemistry could arise in microprobe analyses. Moreover, among the népouite nanoflakes, an amorphous matrix is observed in HR images, which could easily resemble residual silica. Unfortunately, the presence of a pure silica matrix could not be confirmed, because the alternation of nanoflakes and amorphous matrix occurs at a scale that is finer than the TEM-EDS probe size.

The highly-variable oxide totals and, as a consequence, the calculated H_2O contents, are common in Ni-serpentine from other localities analyzed by electron microprobe (Springer 1974; Song et al. 1985; Villanova-de-Benavent et al. 2014). In the present case, the poor crystallinity and the porous microstructure make the samples less dense than the standard used for calibration (metallic Ni).

Always consult and cite the final, published document. See http:/www.minsocam.org or GeoscienceWorld

462 This oddness may potentially generate uncorrected matrix effects, which in turn may be responsible
463 for the low totals.

464 Finally, the Ni-serpentine from Campello Monti shows detectable amounts of S (up to 0.047
465 a.p.f.u.), which seems to be anti-correlated with Si, and thus occupies the tetrahedral site. The
466 presence of S may be related to the leaching of this element out of the parent rock, which contains
467 pyrrhotite, chalcopyrite, and pentlandite (Zucchetti 1979). Its incorporation into garnierite minerals,
468 however, has never been reported before.

469

470 Crystal morphology and structural state of the Ni-serpentine

471 Ni-serpentines usually give poorer diffraction patterns than the corresponding Mg analogues
472 because of their smaller grain size and poorer crystallinity (Brindley and Wan 1975; Brindley 1980)
473 and, unsurprisingly, are even more sensitive to electron beam damage. It has been recognized that
474 the substitution of Ni for Mg causes the structure to be less stable (Brindley and Hang 1973;
475 Poncelet et al. 1979), and it has been observed that the substitution of Ni for Mg in chrysotile gives
476 rise to non-tubular, but also not well-formed platy crystals (Roy and Roy 1954).

477 The Ni-serpentine from Campello Monti forms plumose aggregates made of curved crystals with
478 frayed tips, a few nanometers thick along the stacks and a few tens of nanometer long (nanoflakes).
479 This description is actually intermediate between that of lizardite-like and chrysotile-like phases,
480 even if it is closer to the lizardite-like one. With regard to polytypism, within the limit of the
481 observation of such beam sensitive material, all the possible lizardite stacking sequences have been
482 observed, although most crystals show stacking disorder. The small grain size, the high density of
483 defects, and the intermediate character between the lizardite-like and chrysotile-like phase probably
484 explain the ambiguities that occurred during the characterization of this material. On the contrary,
485 as explained below, it seems plausible that the high Ni content could be responsible for the crystal
486 morphology, i.e. a flat rather than cylindrical habit and a poor crystallinity (high density of defects).

Always consult and cite the final, published document. See http:/www.minsocam.org or GeoscienceWorld

It is generally accepted that that the misfit between the smaller parameter of the tetrahedral sheet and the larger parameter of the octahedral one is the main cause of the cylindrical habit of chrysotile (Bailey 1988), although other authors give different explanations (e.g., Viti and Mellini 1997). Perbost et al. (2003) found a correlation between the curvature of serpentine layers and the misfit between the tetrahedral and octahedral sheets, and thus a dependence with the cation size in the tetrahedral and octahedral positions. Since the ionic radius of $^{[VI]}Ni^{2+}$ (0.69 Å) is lower than that of $^{[VI]}Mg^{2+}$ (0.72 Å) (Shannon 1976), a lower structural mismatch for Ni-serpentine than for Mg-serpentine can be predicted, explaining the absence of cylindrical structures in the Ni-rich serpentine from Campello Monti.

Origin of Ni-serpentine at Campello Monti

The garnierite ore at Campello Monti is extremely rich in Ni, whereas primary minerals and their alteration products in the parent rock, which is only partially serpentinized, do not contain Ni at detectable levels, and Ni-bearing sulfides are sparse.

It is generally accepted that the low content of iron — the Ni-serpentine from Campello Monti is almost iron-free — confirms the supergene origin of garnierite, since iron is largely not soluble under common weathering conditions (Pelletier 1983, 1996; Galí et al. 2012 and references therein). Moreover, the alteration of peridotite is a necessary, but not sufficient, condition for the formation of garnierite: high Ni-contents, such as those of the studied népouite, are possible either as a result of continual chemical reaction of ground water on earlier-formed garnierite (Pecora et al. 1949) or recrystallization of phases able to release a large amount of Ni, such as secondary goethite and hematite (Pelletier 1983).

All of these observations point to the supergene origin of the Ni-serpentine of Campello Monti. The green coatings have probably been deposited by ground-water solutions derived from material subjected to a leaching process. This material cannot be represented by the peridotite on which the

Always consult and cite the final, published document. See http:/www.minsocam.org or GeoscienceWorld

Ni-serpentine has been deposited, since it does not contain appreciable amount of Ni (0.10–0.32 wt. % of NiO, Bertolani 1968; 0.34–0.44 wt. %, Table 1, this study) and does not show signs of further serpentinization. The most likely scenario is thus that late fluids scavenged Ni from nearby altered peridotites and sulfide ores, and deposited less-mobile elements along fractures and voids of the host peridotite just outside their provenance area. Since serpentine and serpentine-népouite s.s. are stable with respect to talc and kerolite-pimelite s.s. at higher $\log[a_{Mg2+} + a_{Ni2+}/a^2_{(H+)}]$ and lower $\log[a_{SiO2}]$ conditions (Bricker et al. 1973; Back et al. 2004; Galí et al. 2012), it is very possible that at Campello Monti a high Ni/SiO_2 activity ratio in the fluids led to the precipitation of népouite instead of a talc-like phase.

Implications

Fundamental research on Ni-bearing hydrous silicates has attracted a great deal of attention in the scientific community during the last few years (e.g., Wells et al. 2009; Suárez et al. 2011; Villanova-de-Benavent et al. 2014, 2016), probably because it provides a spin-off for the many technological applications of Ni-phyllosilicates and because of the importance of the latter as ore for Ni.

Sivaiah et al. (2011) used serpentine-like and talc-like Ni-phyllosilicates as catalyst precursors for processing greenhouse gases such as CO_2 and CH_4. Yang et al. (2011) synthetized Ni-serpentine nanotubes (analogous to pecoraite) with tunable magnetic properties. Moreover, this material has shown promising transport kinetics and discharge capacity when used as the anode in Li-ion batteries. Alencar et al. (2014) synthetized organophilic talc-like Ni-phyllosilicates for the removal of blue dye from textile industry wastewater.

In this study, an unprecedented chemical and structural characterization down to the near-atomic scale of a natural Ni-serpentine is reported, which may be very useful for the design of new technological applications, since it may represent a reference for the synthetic analogues. Moreover,

Always consult and cite the final, published document. See http:/www.minsocam.org or GeoscienceWorld

this study also suggests that natural Ni-phyllosilicates may be directly used as catalyst precursors or starting materials for the synthesis of functionalized devices.

Nickel is extensively used in stainless steel production, in metal plating, in NiMH batteries, coins, etc., and this usage has increased over time in connection with economic development. The continual growth of Ni demand, paralleled by the ongoing depletion of sulfide ores, suggests an increase in the need for Ni production from laterite deposits in the future (Kesler and Simon 2015). Hydrometallurgical ore processing methods, such as acidic leaching, are traditionally used for the extraction of Ni from laterites. However, the speed and percentage recovery of Ni have proven to be variable among different ore bodies, depending on the mineralogy and reactivity of Ni laterites (for a review see McDonald and Whittington 2008). The data indicate that Ni is more readily leached from clay-like ores than limonitic ores. The reason relies on the kinetics and mechanism of acid leaching of laterite minerals. For instance, serpentine minerals dissolve incongruently by partial decomposition of the structure, quickly releasing octahedral cations and leaving a hydrate silica residue, so that the total dissolution of the serpentine is not required for complete Ni extraction. Conversely, in goethite, where small amounts of Ni (up to 7%) can substitute for iron, substantial extraction requires complete dissolution of the goethite grains (Soler et al. 2008; McDonald and Whittington 2008 and references therein).

The development of new hydrometallurgical ore processing methods, which are more effective and economically feasible, requires a greater understanding of the mineralogy, morphology, and texture of the nickel-bearing minerals. Indeed, isomorphic substitutions, crystallinity, and particle size also affect the leaching kinetics of laterite minerals. For instance, chromium and aluminum substitutions stabilize goethite against proton attack (Schwertmann 1991) and mechanical activation (grinding) of laterite ore increases the rate of Ni extraction (Sanchez et al. 1997; Kim and Chung 2002). In particular, dry grinding of garnierite ore induces structural changes that convert serpentine (and other limonitic material) from crystalline to amorphous, which may have beneficial effects on metal extraction, but detrimental effects, i.e. worse settling properties, on downstream processing.

Always consult and cite the final, published document. See http:/www.minsocam.org or GeoscienceWorld

563 This study reveals that the garnierite ore from Campello Monti is among the richest in Ni ever
564 reported. TEM observations suggest that Ni can be easily extracted by acid leaching from
565 octahedral sites at the edges of the curved clay particles with frayed tips. Moreover, the very fine
566 grain size and the high density of defects of the Ni-serpentine offer high surface-to-volume ratio
567 and a high number of reactive sites, which should promote fast acid leaching even without
568 mechanical activation, thus reducing downstream treatment problems. This implies that similar
569 hydrous silicate deposits all around the world may be favorably treated with modern
570 hydrometallurgical methods, and thus represent a possible answer to the continual growth of the
571 demand for Ni. The nanoscale approach used here may be extended to other base metals such as Zn,
572 which may be abundant in phyllosilicates forming similar textures (e.g., Buatier et al. 2016).

573 Overall, it seems that fundamental studies on Ni-bearing hydrous silicates, and especially
574 characterization of these minerals down to the near-atomic scale, may have important implications
575 for the development of new technological applications and new and more efficient ore processing
576 methods, which is required by the continual growth of the demand for Ni, and for other base metals
577 in general.

578

579 **Acknowledgements**

580 Vittorio Mattioli is greatly acknowledged for providing the garnierite samples and Federico
581 Caldiroli for their preliminary characterization during his graduate thesis. Paolo Gentile is greatly
582 acknowledged for assistance during SEM observations and analyses; Lucia Galimberti for EDXRF
583 and XRPD analyses of peridotite; Eleonora Braschi for EMP analyses on garnierite. The paper has
584 greatly benefited from careful revision by two anonymous referees.

585

586 **References**

Always consult and cite the final, published document. See http:/www.minsocam.org or GeoscienceWorld

587 Alencar, J.M., Oliveira, F.J.V.E., Airoldi, C., and Silva Filho, E.C. (2014) Organophilic nickel
588 phyllosilicate for reactive blue dye removal. Chemical Engineering Journal, 236, 332-340.

589 Back, W., Garrido, C.J., Paulick, H., Harvey, J., and Rosner, M. (2004) Seawater-peridotite
590 interactions: First insights from ODP Leg 209, MAR 15 °N. Geochemistry, Geophysics,
591 Geosystem, 5, 1-22.

592 Bailey, S.W. (1988) Introduction. In: Bailey, S.W. (Eds.), Hydrous phyllosilicates (Exclusive of
593 micas), 19, p. 1-8. Reviews in Mineralogy and Geochemistry, Mineralogical Society of America,
594 Washington, D.C.

595 Balan, E., Saitta, A.M., Mauri, F., Lemaire, C., and Guyot, F. (2002) First-principles calculation of
596 the infrared spectrum of lizardite. American Mineralogist, 87, 1286-1290.

597 Baron, F. and Petit, S. (2016) Interpretation of the infrared spectra of the lizardite-nepouite series in
598 the near- and mid-infrared range. American Mineralogist, 101, 423-430.

599 Bertolani, M. (1968) La petrografia della Valle Strona (Alpi Occidentali Italiane). Schweizer
600 Mineralogische und Petrographische Mitteilungen, 48, 3, 695-732.

601 Bertolani, M. (1974) Guida geologico-petrografica della Valsesia-Valsessera e Valle Strona, 123 p.
602 Associazione Pro Natura Valsesia, Varallo.

603 Bish, D.L. and Post, J.E. (1993) Quantitative mineralogical analysis using the Rietveld full-pattern
604 fitting method. American Mineralogist,78, 932-940.

605 Boriani, A. and Sacchi, R. (1973) Geology of the junction between the Ivrea-Verbano and the
606 Strona-Ceneri zones. Memorie dell'Istituto di Geologia e Mineralogia dell'Università di Padova,
607 28, 1-36.

608 Brand, N.W., Butt, C.R.M., and Elias M. (1998) Nickel laterites: classification and features. AGSO
609 Journal of Australian Geology and Geophysics, 17, 81-88.

Always consult and cite the final, published document. See http:/www.minsocam.org or GeoscienceWorld

610 Bricker, O.P., Nesbitt, H.W., and Gunter, W.D. (1973) The stability of talc. American Mineralogist,
611 58, 64-72.

612 Brigatti, M.F., Galli, E., Medici, L., and Poppi, L. (1997) Crystal structure refinement of aluminian
613 lizardite-2H_2. American Mineralogist, 82, 931-935.

614 Brindley, G.W. (1980) The structure and chemistry of hydrous nickel-containing silicate and nickel-
615 aluminium hydroxy minerals. Bullettin de Minéralogie, 103, 161-169.

616 Brindley, G.W. and Hang, P.T. (1973) The nature of garnierites - I: Structures, chemical
617 compositions and color characteristics. Clays and Clay Minerals, 21, 27-40.

618 Brindley, G.W. and Maksimović, Z. (1974) The nature and nomenclature of hydrous nickel-
619 containing silicates. Clay Minerals, 10, 271-277.

620 Brindley, G.W. and Wan, H.M. (1975) Compositions, structures and thermal, behavior of nickel-
621 containing minerals in lizardite-nepouite series. American Mineralogist, 60, 863-871.

622 Buatier, M., Choulet, F., Petit, S., Chassagnon, R., Vennemann, T. (2016) Nature and origin of
623 natural Zn clay minerals from the Bou Arhous Zn ore deposit: Evidence from electron microscopy
624 (SEM-TEM) and stable isotope compositions (H and O). Applied Clay Science, 132-133, 377-390.

625 Butt, C.R.M. and Cluzel, D. (2013) Nickel laterite ore deposits: weathered serpentinites. Elements,
626 9, 123-128.

627 Capitani, G.C. and Mellini, M. (2004) The modulated crystal structure of antigorite: the m = 17
628 polysome. American Mineralogist, 89, 147-158.

629 Capitani, G.C. and Mellini, M. (2006) The crystal structure of the m = 16 antigorite polysome, by
630 single crystal synchrotron diffraction. American Mineralogist, 91, 394-399.

631 Capitani, G.C. and Mellini, M. (2007) High-resolution transmission electron microscopy (HRTEM)
632 investigation of antigorite polysomes (m = 15 to 18). American Mineralogist, 92, 64-71.

Always consult and cite the final, published document. See http:/www.minsocam.org or GeoscienceWorld

633 Capitani, G.C., Schingaro, E., Lacalamita, M., Mesto, E., and Scordari, F. (2016) 2M_2-tobelite
634 single crystals from Ordovician Armorican sandstones (western France): Structural anomalies
635 explained by high resolution and analytical electron microscopy. Mineralogical Magazine, 80, 143-
636 156.

637 Cavallo, A. and Rimoldi, B. (2013) Chrysotile asbestos in serpentinite quarries: a case study in
638 Valmalenco, Central Alps, Northern Italy. Environmental Sciences: Processes and Impacts, 15,
639 1341-1350.

640 Choulet, F., Buatier, M., Barbanson, L., Guégan, R., and Ennaciri, A. (2016) Zinc-rich clays in
641 supergene non-sulfide zinc deposits. Mineralium Deposita, 51, 467-490.

642 Chukanov, N.V. and Chervonnyi, A.D. (2016) Infrared spectroscopy of minerals and related
643 compounds, 1109 p. Springer.

644 Esson, J. and Carlos, L. (1978) The occurrence, mineralogy and chemistry of some garnierites from
645 Brazil. Bulletin du Bureau de Recherches Géologiques et Minières, section II, 3, 263-274.

646 Farmer, V.C. (1974) The Infrared Spectra of Minerals, 539 p. The Mineralogical Society, London.

647 Faust, G.T. (1966) The hydrous nickel-magnesium silicates – The Garnierite group. American
648 Mineralogist, 51, 279-297.

649 Faust, G.T., Fahey, J.J., Mason, B., and Dwornik, E.J. (1969) Pecoraite, $Ni_6Si_4O_{10}(OH)_9$, nickel
650 analog of clinochrysotile, formed in the Wolf Creek meteorite. Science, 165, 59-60.

651 Fregola, R.A., Capitani, G.C., Scandale, E., and Ottolini, L. (2009) Chemical control on 3T stacking
652 order in a Li-poor biotite mica. American Mineralogist, 94, 334-344.

653 Fritsch, E., Juillot, F., Dublet, G., Fonteneau, L., Fandeur, D., Martin, E., Caner, L., Auzende, A.L.,
654 Grauby, O., and Beaufort, D. (2016) An alternative model for the formation of hydrous Mg/Ni layer
655 silicates ("deweylite"/"garnierite") in faulted peridotites of New Caledonia: I. Texture and

Always consult and cite the final, published document. See http:/www.minsocam.org or GeoscienceWorld

mineralogy of a paragenetic succession of silicate infillings. European Journal of Mineralogy, 28, 295-311.

Galí, S., Soler, J.M., Proenza, J.A., Lewis, J.F., Cama, J., and Tauler, E. (2012) Ni enrichment and stability of Al-free garnierite solid-solutions: A thermodynamic approach. Clays and Caly Minerals, 60, 121-135.

Hill, R.J. (1991) Expanded use of the Rietveld method in studies of phase abundance in multiphase mixtures. Powder Diffraction, 6, 74-77.

Kerrick, D. (2002) Serpentinite Seduction. Science, 298, 1344-1345.

Kesler, E.K. and Simon, A.C. (2015) Mineral Resources, Economics and the Environment, 434 p. Cambridge University Press.

Kilaas, R. (1998) Optimal and near-optimal filters in high-resolution electron microscopy. Journal of Microscopy, 190, 45-51.

Kim, D.-J. and Chung, H.-S. (2002) Effect of grinding on the structure and chemical extraction of metals from serpentine. Particulate Science and Technology, 20, 159-168.

Kogure, T. (2002) Investigations of micas using advanced transmission electron microscopy. In: Mottana, A., Sassi, F.P., Thompson Jr., J.B., and Guggenheim, S. (eds.), Micas: Crystal Chemistry and Metamorphic Petrology, 46, p. 281-312, Reviews in Mineralogy and Geochemistry, Mineralogical Society of America, Chantilly, Virginia.

Larson, A.C. and Von Dreele, R.B. (2004) General Structure Analysis System (GSAS). Los Alamos National Laboratory Report LAUR 86-748.

McDonald, R.G. and Whittington, B.I. (2008) Atmospheric acid leaching of nickel laterites review. Part I. Sulphuric acid technologies. Hydrometallurgy, 91, 35-55.

Mellini, M. (1982) The crystal structure of lizardite 1*T*: hydrogen bonds and polytypism. American Mineralogist, 67, 587-598.

Always consult and cite the final, published document. See http:/www.minsocam.org or GeoscienceWorld

Mellini, M. and Zanazzi, P.F. (1987) Crystal structure of lizardite–1*T* and lizardite–2H_1 from Coli, Italy. American Mineralogist, 72, 943-948.

Mével, C. (2003) Serpentinization of abyssal peridotites at mid-ocean ridges. Comptes Rendus Geoscience, 335, 825-852.

Milton, C., Dwornik, E.J., and Finkelman, R.B. (1983) Pecoraite, the nickel analogue of chrysotile, $Ni_3Si_2O_5(OH)_4$ from Missouri. Neues Jahrbuch für Mineralogie - Monatshefte, 11, 513-523.

Mitchell, D.R. (2007) HRTEM filter. DigitalMicrograph™ Scripting. Available: http://www.dmscripting.com/hrtem_filter.html (accessed September 22, 2017).

Mugnaioli, E., Logar, M., Mellini, M., and Viti, C. (2007) Complexity in 15- and 30-sectors polygonal serpentine: Longitudinal sections, intrasector stacking faults and XRPD satellites. American Mineralogist, 92, 603-616.

Pecora, W.T., Hobbs, S.W., and Murata, J.K. (1949) Variations in garnierite from the nickel deposit near Riddle, Oregon. Economic Geology, 44, 13-23.

Pelletier, B. (1983) Localization du nickel dans les minerais "garnieritiques" de Nouvelle-Calédonie. Sciences Géologique: Mémoire, 73, 173-183.

Pelletier, B. (1996) Serpentines in nickel silicate ore from New Caledonia. Australasian Institute of Mining and Metallurgy publication series – Nickel conference "Mineral to Market", Kalgoorlie. Western Australia, 6(96), 197-205.

Perbost, R., Amouric, M., and Olives, J. (2003) Influence of cation size on the curvature of serpentine minerals: HRTEM-AEM study and elastic theory. Clays and Clay Minerals, 51, 430-438.

Pichou, J.L. and Pichoir, F. (1984) A new model for quantitative X-ray microanalysis. Part I: application to the analysis of homogeneous samples. La Recherche Aerospatiale, 3, 13-38.

Always consult and cite the final, published document. See http:/www.minsocam.org or GeoscienceWorld

Poncelet, G., Jacobs, P., Delannay, F., Genet, M., Gerard, P., and Herbillon, A. (1979) Étude préliminaire sur la localisation du nickel dans une garniérite naturelle. Bulletin de Minéralogie, 102, 379-385.

Reed, S.J.B. (2005) Electron Microprobe Analysis and Scanning Electron Microscopy in Geology, 189 p., Cambridge University Press.

Reynolds, R.C. (1968) The effect of particle size on apparent lattice spacings. Acta Crystallographica, A24, 319-320.

Ridley, J. (2013) Ore Deposit Geology. Cambridge University Press, 398 pp.

Roy, D.M. and Roy, R. (1954) An experimental study of the formation and properties of synthetic serpentine and related layer silicate minerals. American Mineralogist, 39, 957-975.

Sanchez, E.C., Saito, F., and Horita, H. (1997) Enhancement of magnesium and nickel extraction from garnierite by mechanochemical treatment. Shigen-to-Sozai, 113, 35-38.

Sivaiah, M.V., Petit, S., Beaufort, M.F., Eyidi, D., Barrault, J., Batiot-Dupeyrat, C., and Valange, S. (2011) Nickel based catalysts derived from hydrothermally synthesized 1:1 and 2:1 phyllosilicates as precursors for carbon dioxide reforming of methane. Microporous and Mesoporous Materials 140, 69–80.

Schwertmann, U. (1991) Solubility and dissolution of iron oxides. Plant and Soil, 130, 1-25.

Shannon, R.D. (1976) Revised effective ionic radii and systematic studies of interatomic distances in halides and chalcogenides. Acta Crystallographica, A32, 751-767.

Soler, J.M., Cama, J., Galí, S., Meléndez, W., Ramírez, A., and Estanga, J. (2008) Composition and dissolution kinetics of garnierite from the Loma de Hierro Ni-laterite deposit, Venezuela. Chemical Geology, 249, 191-202.

Song, Y., Moon, H.S., and Chon, H.T. (1995) New occurrence and characterization of Ni-serpentines in the Kwangcheon area, Korea. Clay Minerals, 30, 211-224.

Always consult and cite the final, published document. See http:/www.minsocam.org or GeoscienceWorld

726 Springer, G. (1974) Compositional and structural variations in garnierites. Canadian Mineralogist,
727 12, 381-388.

728 Suárez, S., Nieto, F., Velasco, F., and Martín, F.J. (2011) Serpentine and chlorite as effective Ni-Cu
729 sinks during weathering of the Aguablanca sulphide deposit (SW Spain). TEM evidence for metal-
730 retention mechanisms in sheet silicates. European Journal of Mineralogy, 23, 179-196.

731 Van Cappellen, E. and Doukhan, J.C. (1994) Quantitative transmission X-ray microanalysis of ionic
732 compounds. Ultramicroscopy, 53, 343-349.

733 Villanova-de-Benavent, C., Nieto, F., Viti, C., Proenza, J.A., Galí, S., and Roqué-Rosell, J. (2016)
734 Ni-phyllosilicates (garnierites) from the Falcondo Ni-laterite deposit (Dominican Republic):
735 Mineralogy, nanotextures and formation mechanism by HRTEM and AEM. American
736 Mineralogist, 101, 1460-1473.

737 Villanova-de-Benavent, C., Proenza, J.A., Galí, S., García-Casco, A., Tauler, E., Lewis, J.F., and
738 Longo, F. (2014) Garnierites and garnierites: Texture, mineralogy and geochemistry of garnierites
739 in the Falcondo Ni-laterite deposit, Domenican Republic. Ore Geology Reviews, 58, 91-109.

740 Viti, C. and Mellini, M. (1997) Contrasting chemical composition in associated lizardite and
741 chrysotile in veins from Elba, Italy. European Journal of Mineralogy, 9, 585-596.

742 Wells, M.A., Ramanaidou, E.R., Verrall, M., and Tessarolo, C. (2009) Mineralogy and crystal
743 chemistry of garnierites in the Goro lateritic nickel deposit, New Caledonia. European Journal of
744 Mineralogy, 21, 467-483.

745 Yang, Y., Liang, Q., Li, J., Zhuang, Y., He, Y., Bai, B., and Wang, X. (2011) $Ni_3Si_2O_5(OH)_4$ multi-
746 walled nanotubes with tunable magnetic properties and their application as anode materials for
747 lithium batteries. Nano Research, 4, 882-890.

748 Zanoletti, E. (2007) Il patrimonio geologico della Valle Strona (VB): un'opportunità per il turismo.
749 Atti del 3° Congresso di Geologia & Turismo, Bologna (Italy).

Always consult and cite the final, published document. See http:/www.minsocam.org or GeoscienceWorld

Zhang, F., Chan, S.W., Spanier, J.E., Apak, E., Jin, Q., Robinson, R.D., and Herman, I.P. (2002) Cerium oxide nanoparticles: size-selective formation and structure analysis. Applied Physics Letters, 80, 127-129.

Zucchetti, S. (1979) Remarks on the nickel deposits of the Western Alps (Italy). Proceedings of the 3rd International Symposium on the Mineral Deposits of the Alps (ISMIDA), Loeben 1977, 355-360. Verhandlungen der Geologischen Bundesanstalt, 3, 529-534.

Caption to Figures and Tables

Figure 1. Geological map of the Strona Valley (modified after Bertolani 1974).

Figure 2. Left: hand specimen of garnierite from Campello Monti used in this study (sample ~13 cm wide); right: stereomicrograph of the green, thin coating separated from the hand specimen (micrograph side ~0.5 mm).

Figure 3. Optical and electron microscopy images of peridotite (scale bar 0.5 mm if not differently specified): a) crossed polars image and b) backscattered electron (BSE) image of olivine (Ol), orthopyroxene (Opx), and spinel (Spl) forming a coarse granular texture. Note the magnetite strings (Mag) along fractures possibly produced by incipient serpentinization; c) crossed polars image; and d) BSE image of altered spinel grains with a corona texture of chlorite (Chl) and a rim of Cr-rich magnetite (Cr-Mag). The orthopyroxene embedding spinel and chlorite is partially substituted by serpentine (Srp) and magnetite (Mag). A small clinopyroxene grain (Cpx), completes the local mineral association; crossed polars images of orthopyroxene e) partially replaced along fractures by talc (Tlc), and f) olivine and spinel partially altered to serpentine and chlorite, respectively; g) BSE image (Pn) and pyrrhotite (Po) rimmed by Fe-oxides (Fe-Ox) within partially serpentinized harzburgite (black).

Always consult and cite the final, published document. See http:/www.minsocam.org or GeoscienceWorld

Figure 4. Optical micrographs of garnierite (scale bar 0.5 mm): a) parallel light image and (b) crossed polars image of the green coating; c) parallel light image of a cross section through the garnierite coating (green) and the host rock (lower part). The opaque minerals are mostly iron oxides (black) and hydroxides (reddish); d) single polar image of a garnierite vein intruding the host rock. Note the colorless Mg-serpentine (Srp) bordering the vein and altering the surrounding olivine (Ol).

Figure 5. BSE images of two selected areas from sample GC1 a) and GC3 b) analyzed using the WDS microprobe. Dotted lines limit three different zones, indicated by numbers 1, 2, and 3, characterized by different microstructure/composition (for explanation see text). L-L' lines represent the traces of the major element intensity profiles shown in c) for sample GC1 and in d) for sample GC3. Spot analyses were acquired in EDS mode at steps of ~0.18 μm using a counting time of 5 s per step.

Figure 6. Binary plots showing the compositional correlations in Ni-serpentine from Campello Monti: a) Mg vs. Ni; b) Cu vs. Ni; c) S vs. Si and d) ternary Mg-Si-Ni diagram. Dashed lines represent compositional trends. Lz = lizardite [$(Mg_3Si_2O_5(OH)_4$], Nep = népouite [$(Ni_3Si_2O_5(OH)_4$], Krp = "karpinskite" [$Mg_2Si_2O_5(OH)_2$], Ni-Krp = "Ni-karpinskite" [$Ni_2Si_2O_5(OH)_2$], Tlc = talc [$Mg_3Si_4O_{10}(OH)_2$], Wil = willemseite [$(Ni_3Si_4O_{10}(OH)_2$], Sep = sepiolite [$Mg_4Si_6O_{15}(OH)_2 \cdot 6H_2O$], Fal = falcondoite [$Ni_4Si_6O_{15}(OH)_2 \cdot 6H_2O$].

Figure 7. X-ray powder diffractogram of Ni-serpentine from Campello Monti (left), to be compared with the Ni-serpentine from Kwangcheon, Korea (inset, Song et al. 1995). Note the presence of only one strong peak in the region 1.50–1.54 Å (61.8–60.0° 2θ), unlike the diffractogram of dimorphous népouite, which shows two intense peaks in this "critical" region.

Figure 8. Infrared spectrum of the Ni-serpentine from Campello Monti in comparison with the spectrum of népouite from Petea Mine (Soroako, Sulawesi Island, Indonesia) and that of pecoraite from Loma Peguera (Bonao, Dominican Republic), taken as reference (Chukanov and Chervonnyi 2016).

Always consult and cite the final, published document. See http:/www.minsocam.org or GeoscienceWorld

Figure 9. a) Low magnification TEM image of népouite; b) Lattice fringe image of the same area showing nanoflakes with one-layer periodicity. Note the close resemblance of Fig. 9a to Figure 5c of Villanova-de-Benavent et al. (2016), although they refer to two different phases, namely a 7-Å phase and a 10-Å phase, respectively; c) SAED pattern of a) and related radial profile d) with indication of the measured interplanar distances.

Figure 10. HR image simulation along ⟨110⟩ of three népouite polytypes derived from the three 1*T*, $2H_1$ and $2H_2$ lizardite polytypes. Relevant Blochwave simulation parameters: atomic potential = Bethe; atomic form factors = PRDW (Peng-Ren-Dudarev-Whelan); n. of strong reflections = 50; sample thickness = 4 nm; defocus = 42.5 nm; spherical aberration = 0.5 mm; chromatic aberration = 1 mm; convergence semi-angle = 1 mrad; defocus spread = 3.5 nm; energy spread = 1.40 eV; objective aperture = 5.2 nm^{-1}.

Figure 11. HR filtered (average background subtracted) images of népouite crystals: a) and b) refer to the same TEM image, as well as c) and d); only a drawing of the direct lattice has been added to b) and d) to emphasize the stacking. Note the local straight sequence to the left and the presence of a dislocation-like defect in the bent region to the right (b) and the local zig-zag sequence (d).

Figure 12. a) HR filtered (average background subtracted) image of népouite showing many nanoflakes with preserved two-dimensional information; b) and c) enlargement of the square regions indicated in a), further filtered in the Fourier space using a periodical mask, and with drawings to emphasize the stacking. Note the disordered sequence in b) showing stacking to the left (l), straight (s), and to the right (r) in short succession. In c) the closure gap in the lattice circuit probably discloses a dislocation-like defect.

Table 1. EDXRF bulk analyses of the garnierite ultramafic host rock.

Table 2. WDS-EMP analyses of Ni-serpentine from Campello Monti (averages and ranges) carried out on the intermediate zones (zone 2 in Fig. 5) of three different samples and distinguished

Always consult and cite the final, published document. See http:/www.minsocam.org or GeoscienceWorld

826 according to their backscattered electron (BSE) contrast (analyses calculated on the basis of seven
827 oxygens).
828 Table 3. WDS-EMP spot analyses referring to Ni-serpentine from the inner and outer zones (zone 1
829 and zone 3 in Fig. 5, respectively) and to the most deviating compositions found in the outer zone
830 (analyses calculated on the basis of 7 oxygens).
831 Table 4. XRPD data and crystallographic parameters of the Ni-serpentine from Campello Monti as
832 compared with pecoraite and népouite from Kwangcheon, Korea (Song et al. 1995).
833 Table 5. Positions (cm^{-1}) and proposed assignment for peaks observed in the FTIR spectra of the
834 Ni-serpentine from Campello Monti.

Always consult and cite the final, published document. See http:/www.minsocam.org or GeoscienceWorld

This is a preprint, the final version is subject to change, of the American Mineralogist (MSA)
Cite as Authors (Year) Title. American Mineralogist, in press.
DOI: https://doi.org/10.2138/am-2018-6229

FIGURE 1

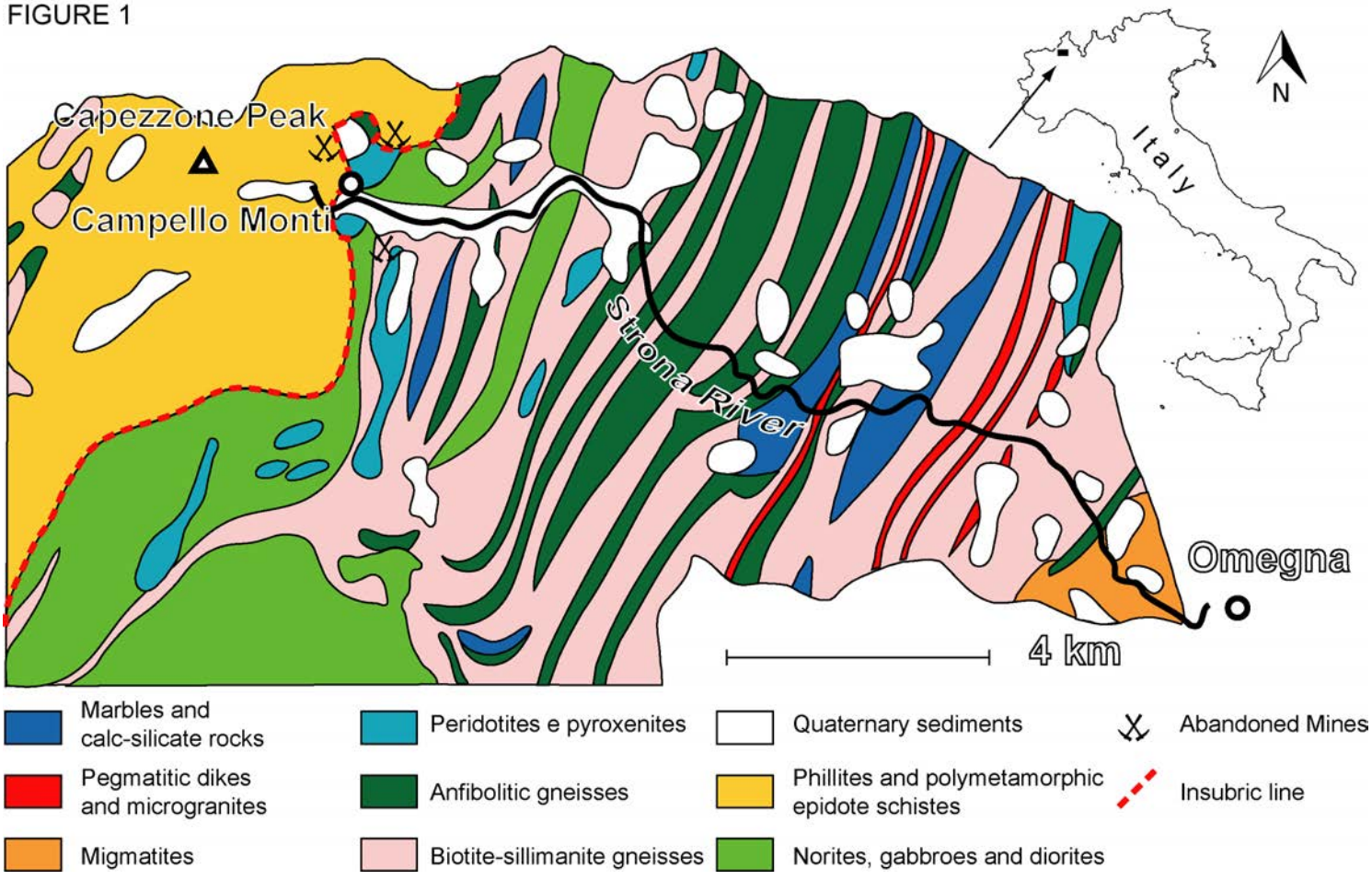

Always consult and cite the final, published document. See http:/www.minsocam.org or GeoscienceWorld

This is a preprint, the final version is subject to change, of the American Mineralogist (MSA)
Cite as Authors (Year) Title. American Mineralogist, in press.
DOI: https://doi.org/10.2138/am-2018-6229

Figure 2

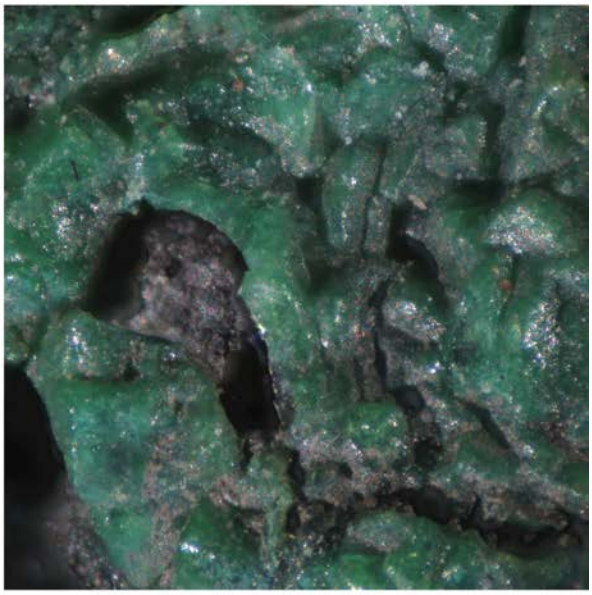

Always consult and cite the final, published document. See http:/www.minsocam.org or GeoscienceWorld

This is a preprint, the final version is subject to change, of the American Mineralogist (MSA)
Cite as Authors (Year) Title. American Mineralogist, in press.
DOI: https://doi.org/10.2138/am-2018-6229

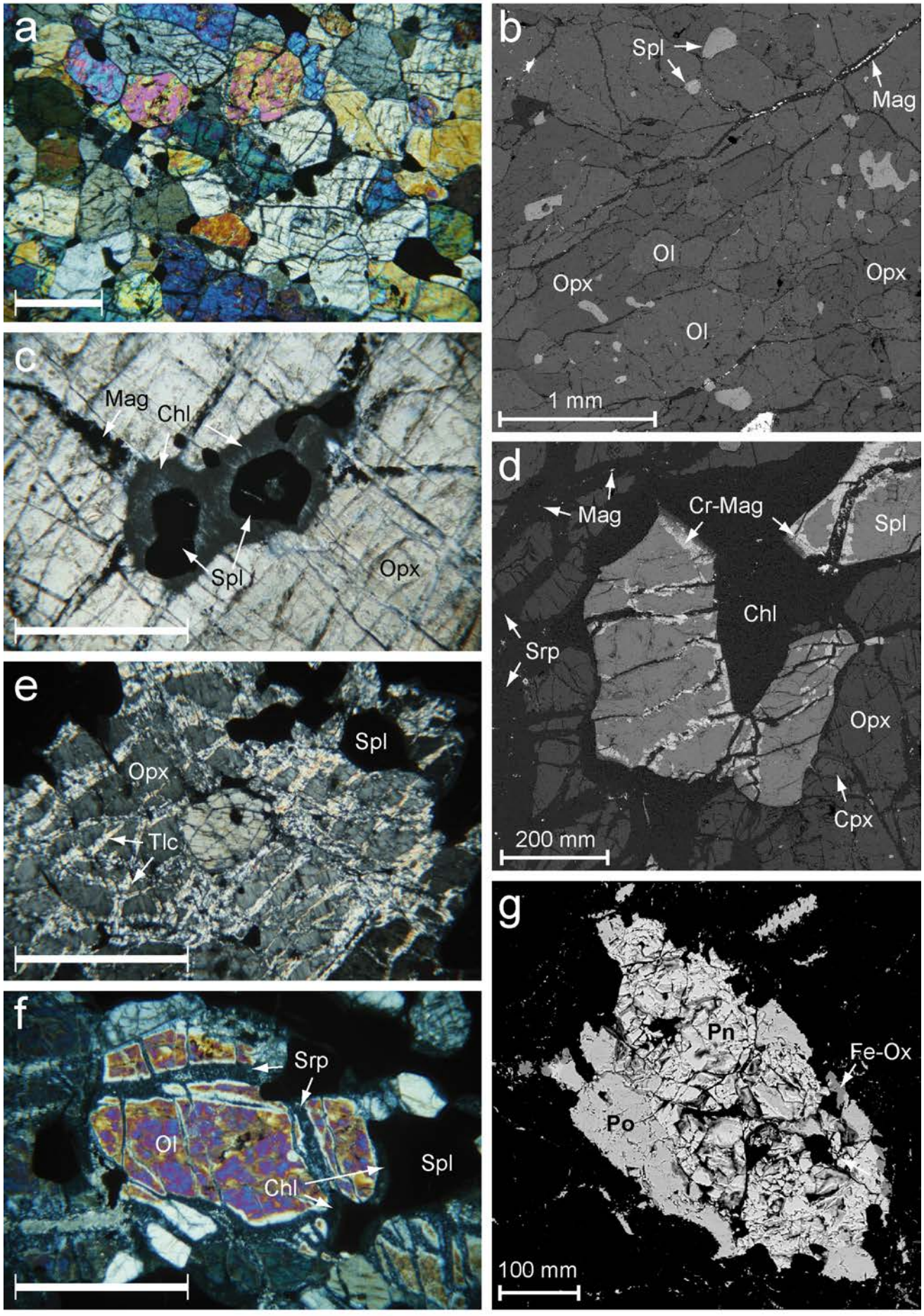

FIGURE 3

Always consult and cite the final, published document. See http:/www.minsocam.org or GeoscienceWorld

This is a preprint, the final version is subject to change, of the American Mineralogist (MSA)
Cite as Authors (Year) Title. American Mineralogist, in press.
DOI: https://doi.org/10.2138/am-2018-6229

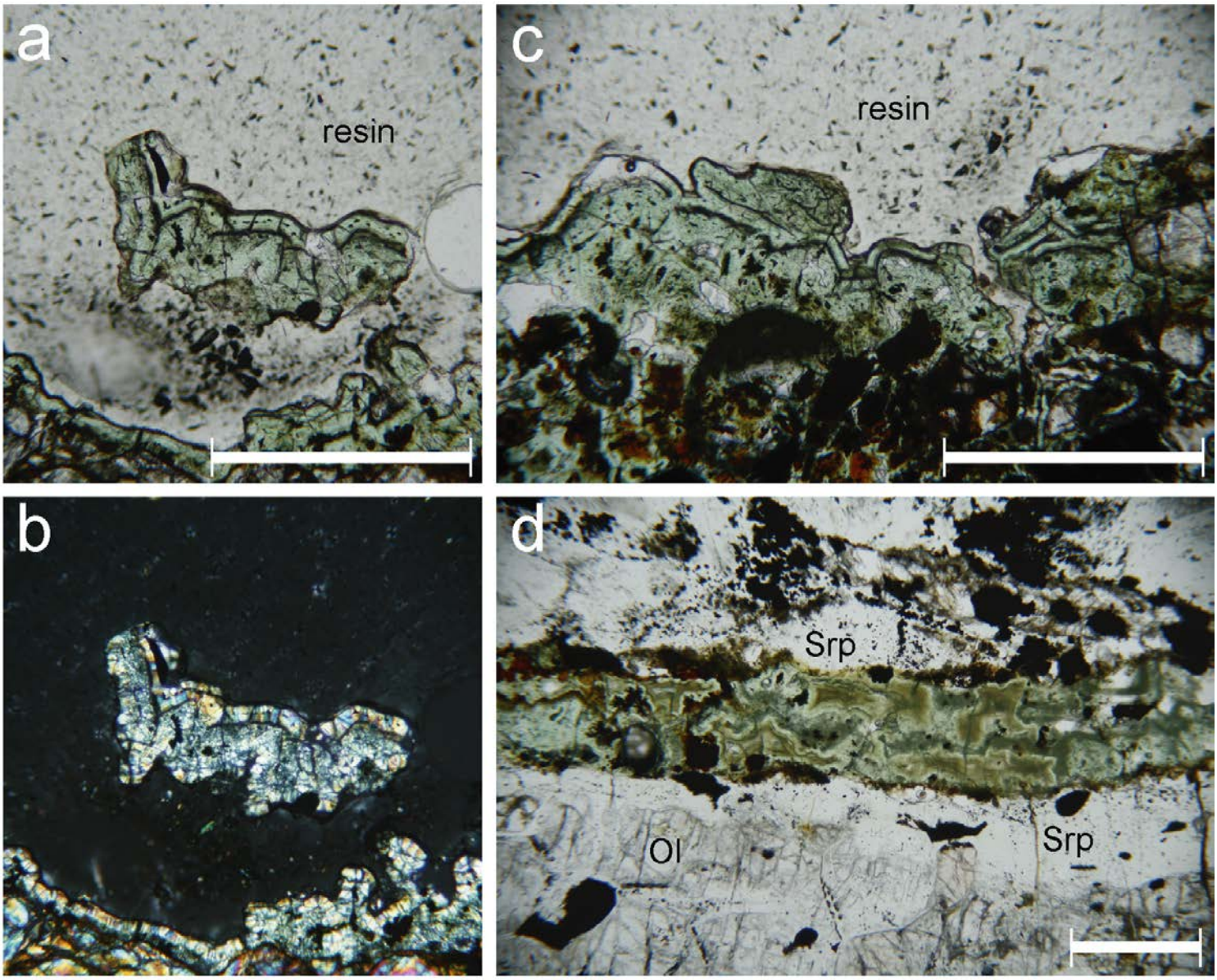

FIGURE 4

Always consult and cite the final, published document. See http:/www.minsocam.org or GeoscienceWorld

This is a preprint, the final version is subject to change, of the American Mineralogist (MSA)
Cite as Authors (Year) Title. American Mineralogist, in press.
DOI: https://doi.org/10.2138/am-2018-6229

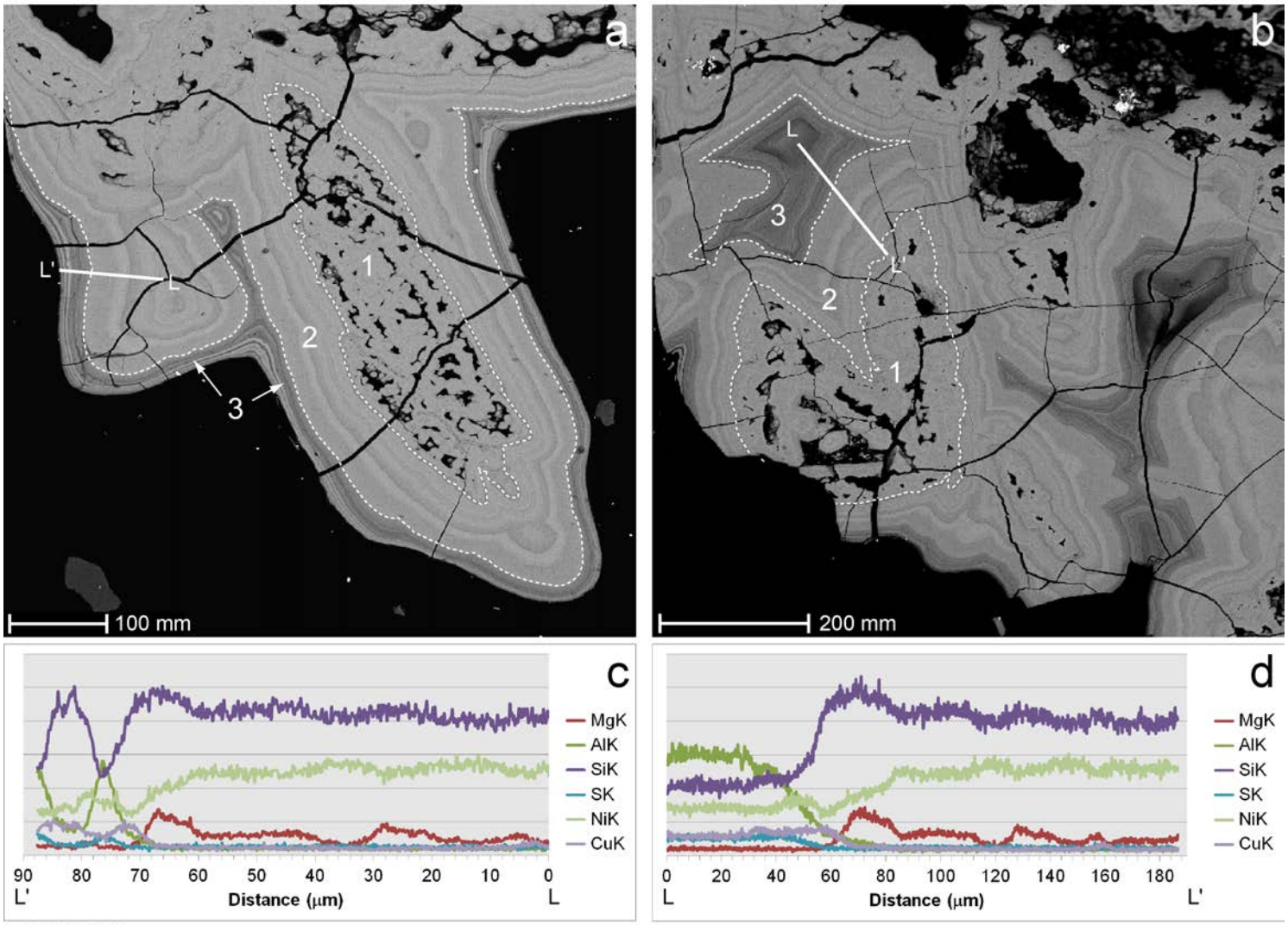

FIGURE 5

Always consult and cite the final, published document. See http:/www.minsocam.org or GeoscienceWorld

This is a preprint, the final version is subject to change, of the American Mineralogist (MSA)
Cite as Authors (Year) Title. American Mineralogist, in press.
DOI: https://doi.org/10.2138/am-2018-6229

Figure 6

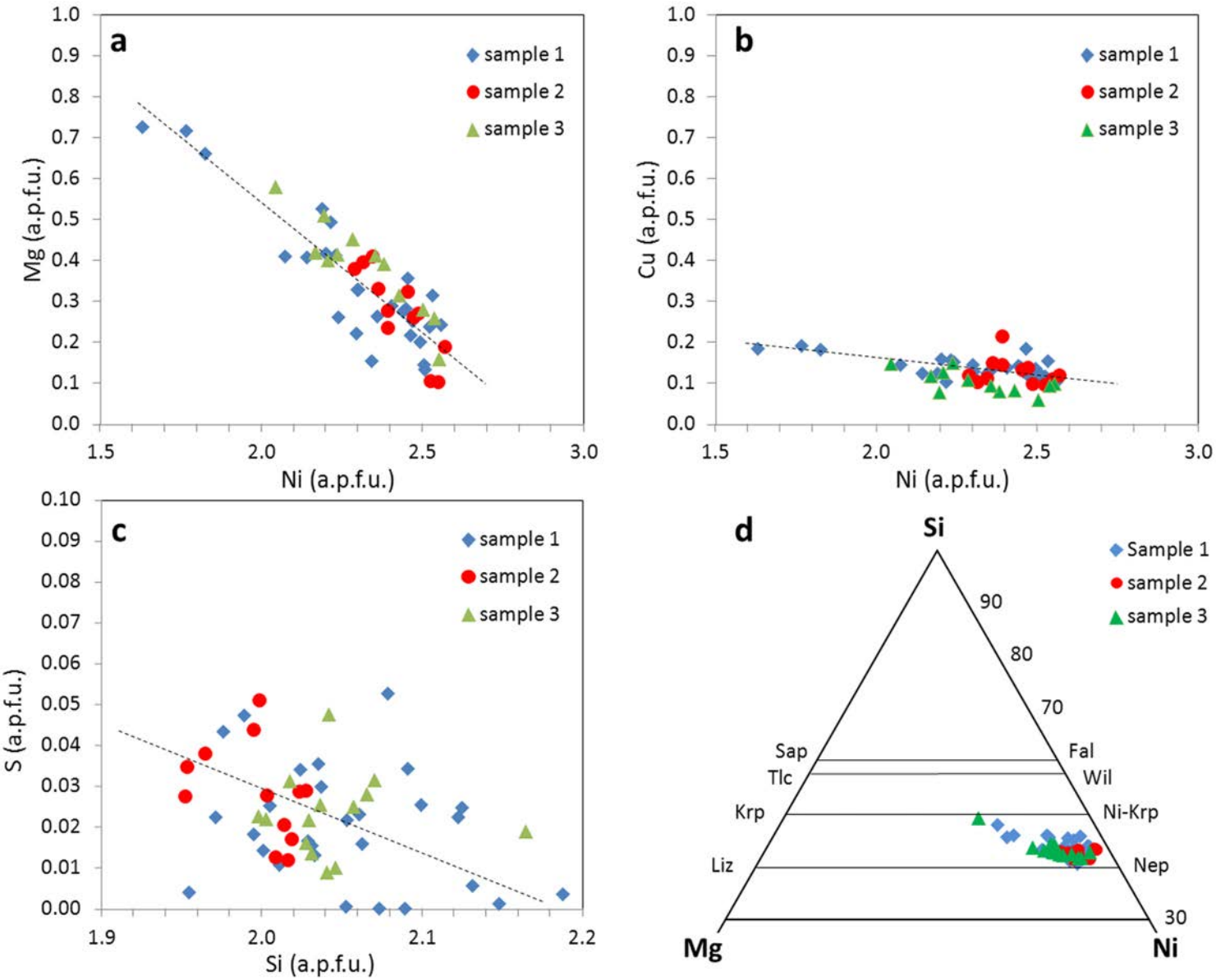

Always consult and cite the final, published document. See http:/www.minsocam.org or GeoscienceWorld

This is a preprint, the final version is subject to change, of the American Mineralogist (MSA)
Cite as Authors (Year) Title. American Mineralogist, in press.
DOI: https://doi.org/10.2138/am-2018-6229

Figure 7

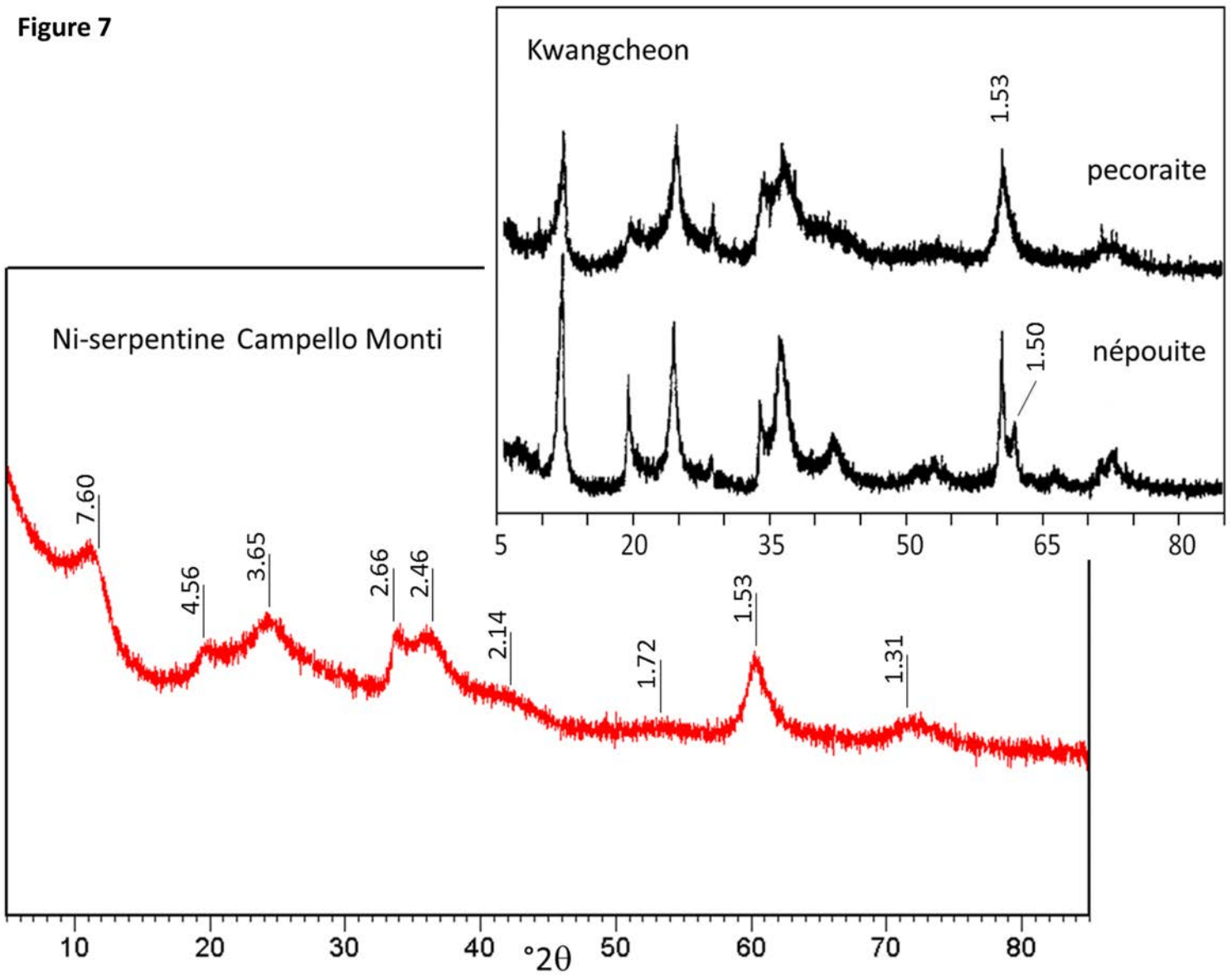

Always consult and cite the final, published document. See http:/www.minsocam.org or GeoscienceWorld

This is a preprint, the final version is subject to change, of the American Mineralogist (MSA)
Cite as Authors (Year) Title. American Mineralogist, in press.
DOI: https://doi.org/10.2138/am-2018-6229

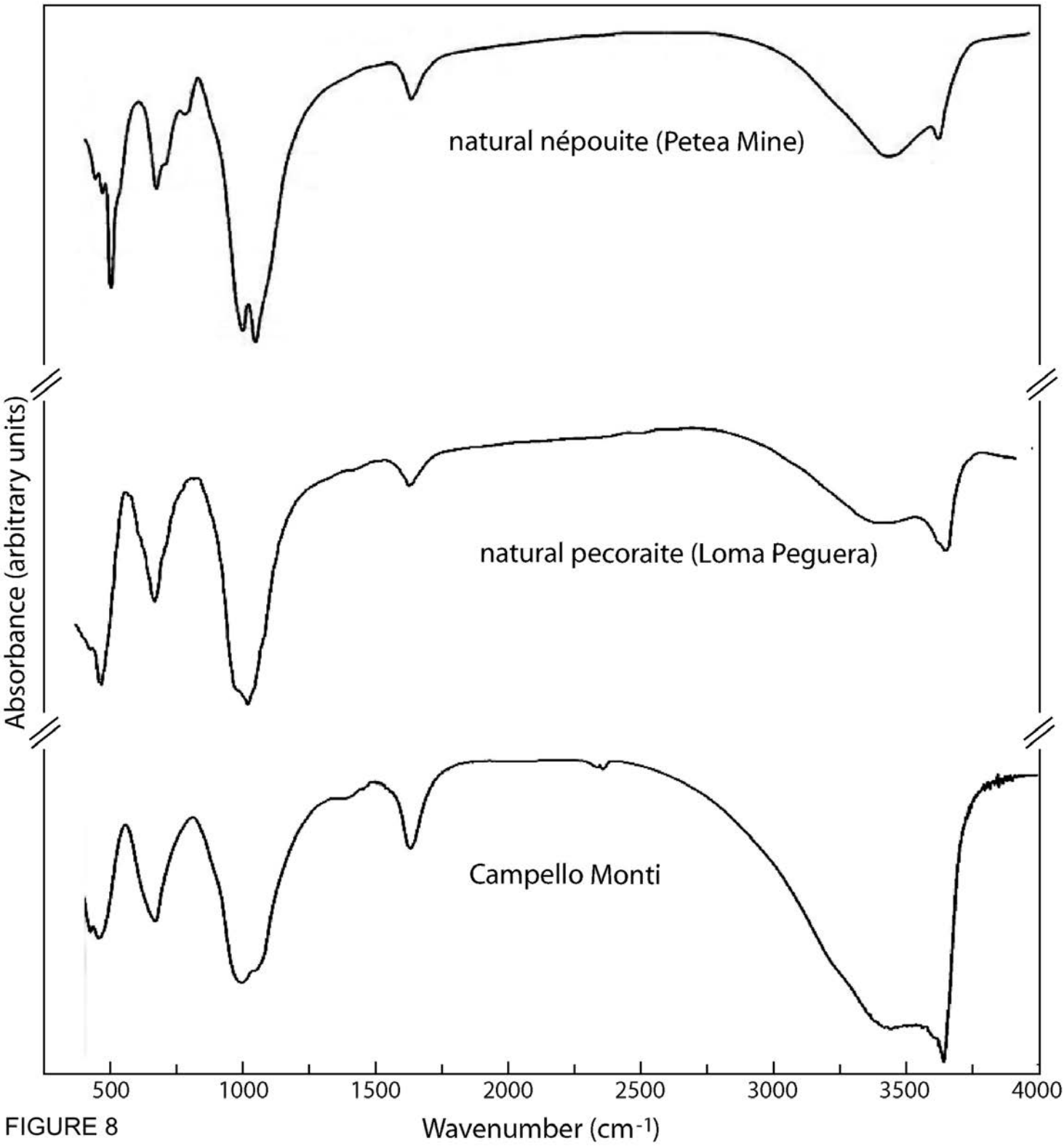

FIGURE 8

Always consult and cite the final, published document. See http:/www.minsocam.org or GeoscienceWorld

This is a preprint, the final version is subject to change, of the American Mineralogist (MSA)
Cite as Authors (Year) Title. American Mineralogist, in press.
DOI: https://doi.org/10.2138/am-2018-6229

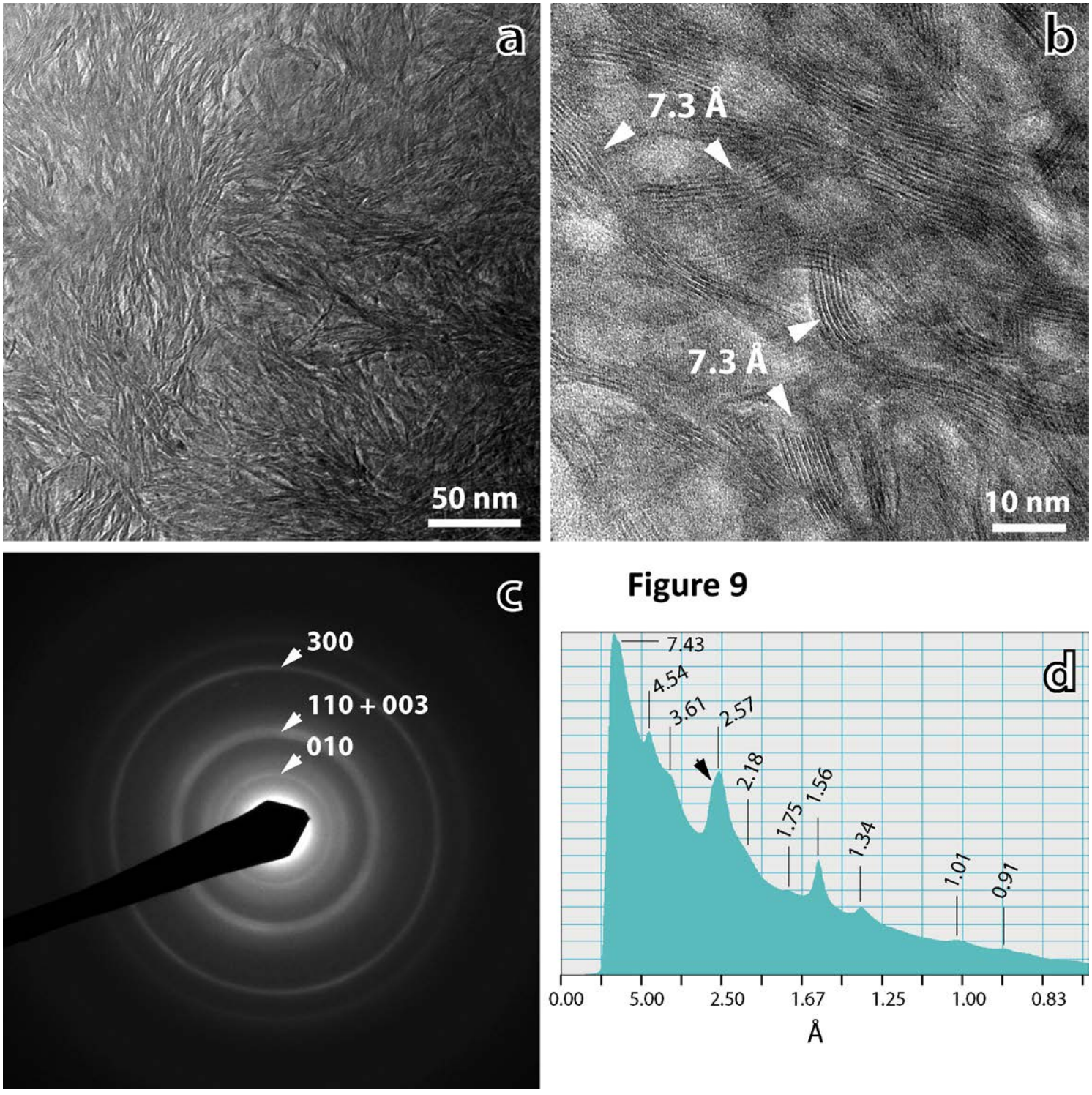

Figure 9

Always consult and cite the final, published document. See http:/www.minsocam.org or GeoscienceWorld

This is a preprint, the final version is subject to change, of the American Mineralogist (MSA)
Cite as Authors (Year) Title. American Mineralogist, in press.
DOI: https://doi.org/10.2138/am-2018-6229

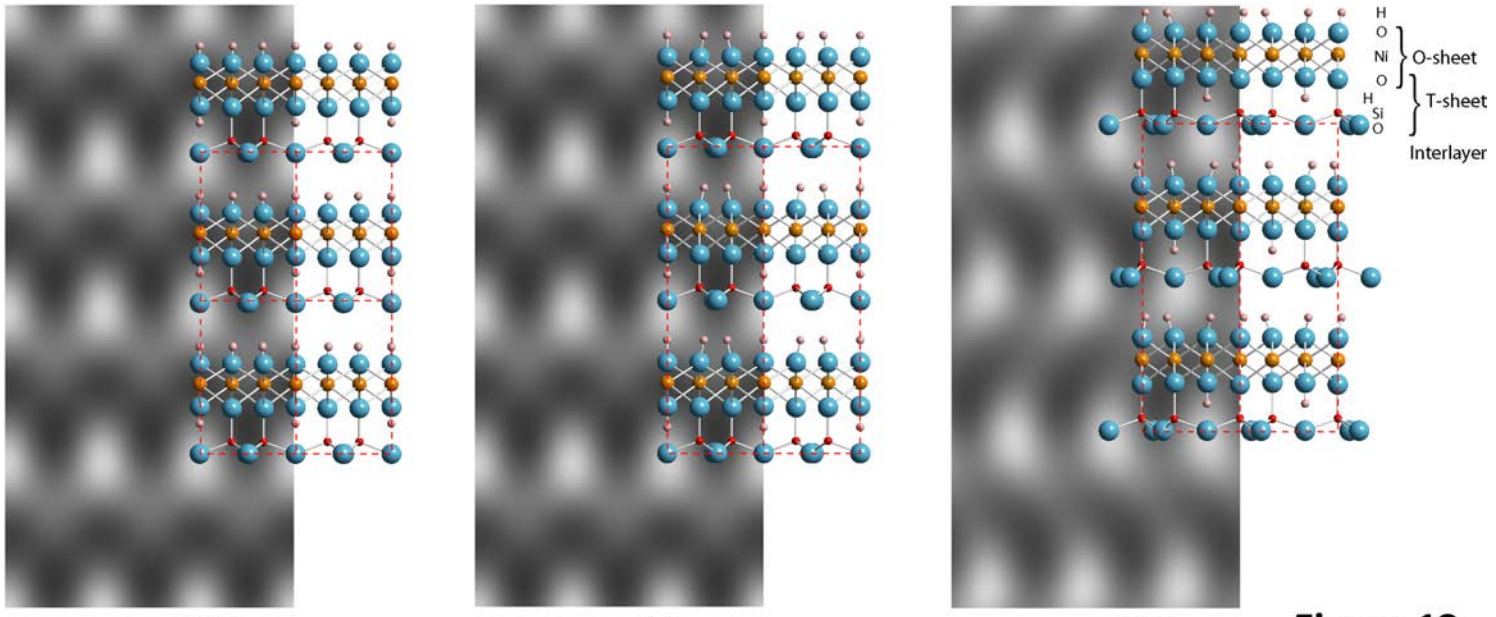

Figure 10

Always consult and cite the final, published document. See http:/www.minsocam.org or GeoscienceWorld

This is a preprint, the final version is subject to change, of the American Mineralogist (MSA)
Cite as Authors (Year) Title. American Mineralogist, in press.
DOI: https://doi.org/10.2138/am-2018-6229

Figure 11

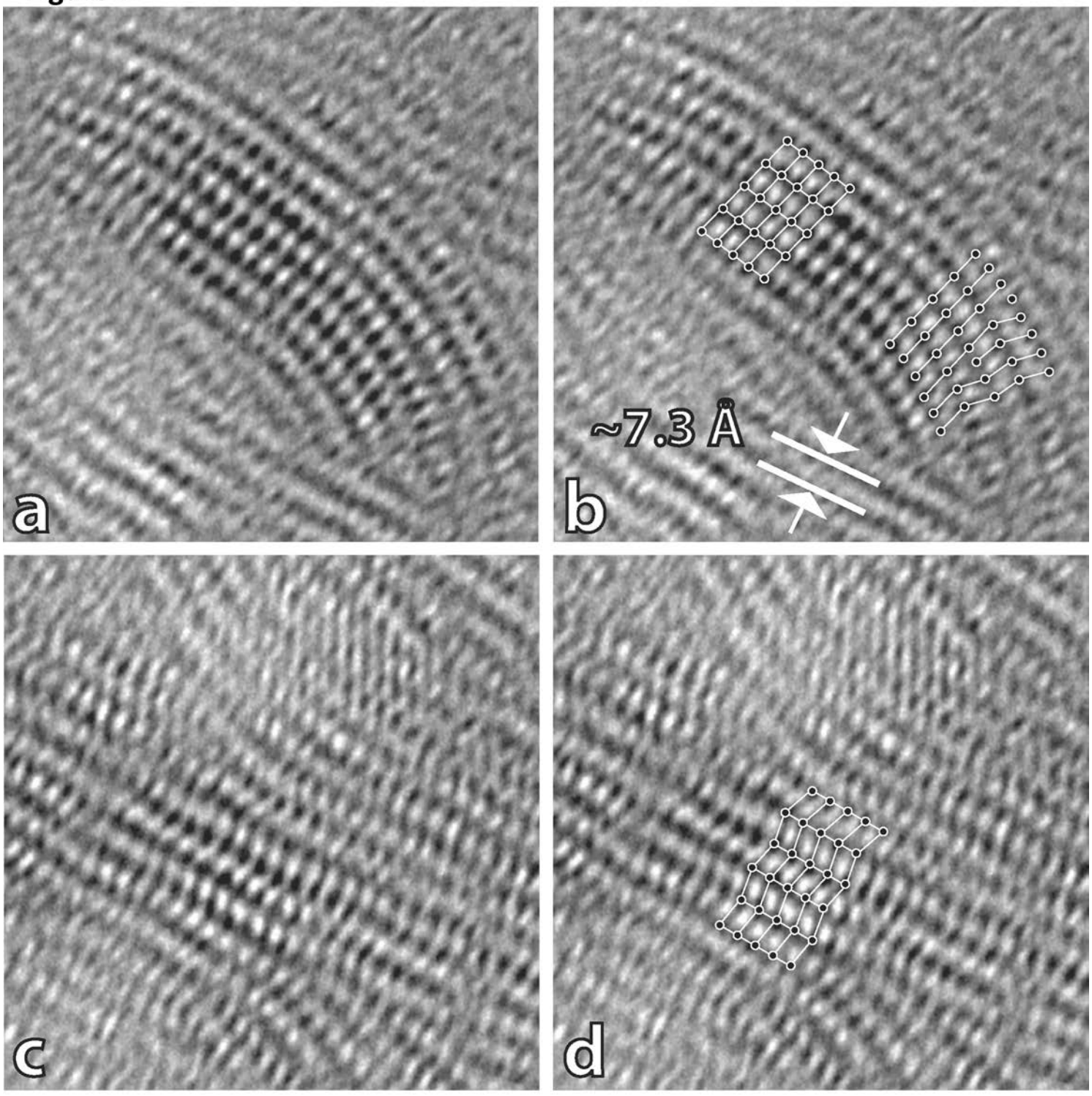

Always consult and cite the final, published document. See http:/www.minsocam.org or GeoscienceWorld

This is a preprint, the final version is subject to change, of the American Mineralogist (MSA)
Cite as Authors (Year) Title. American Mineralogist, in press.
DOI: https://doi.org/10.2138/am-2018-6229

Figure 12

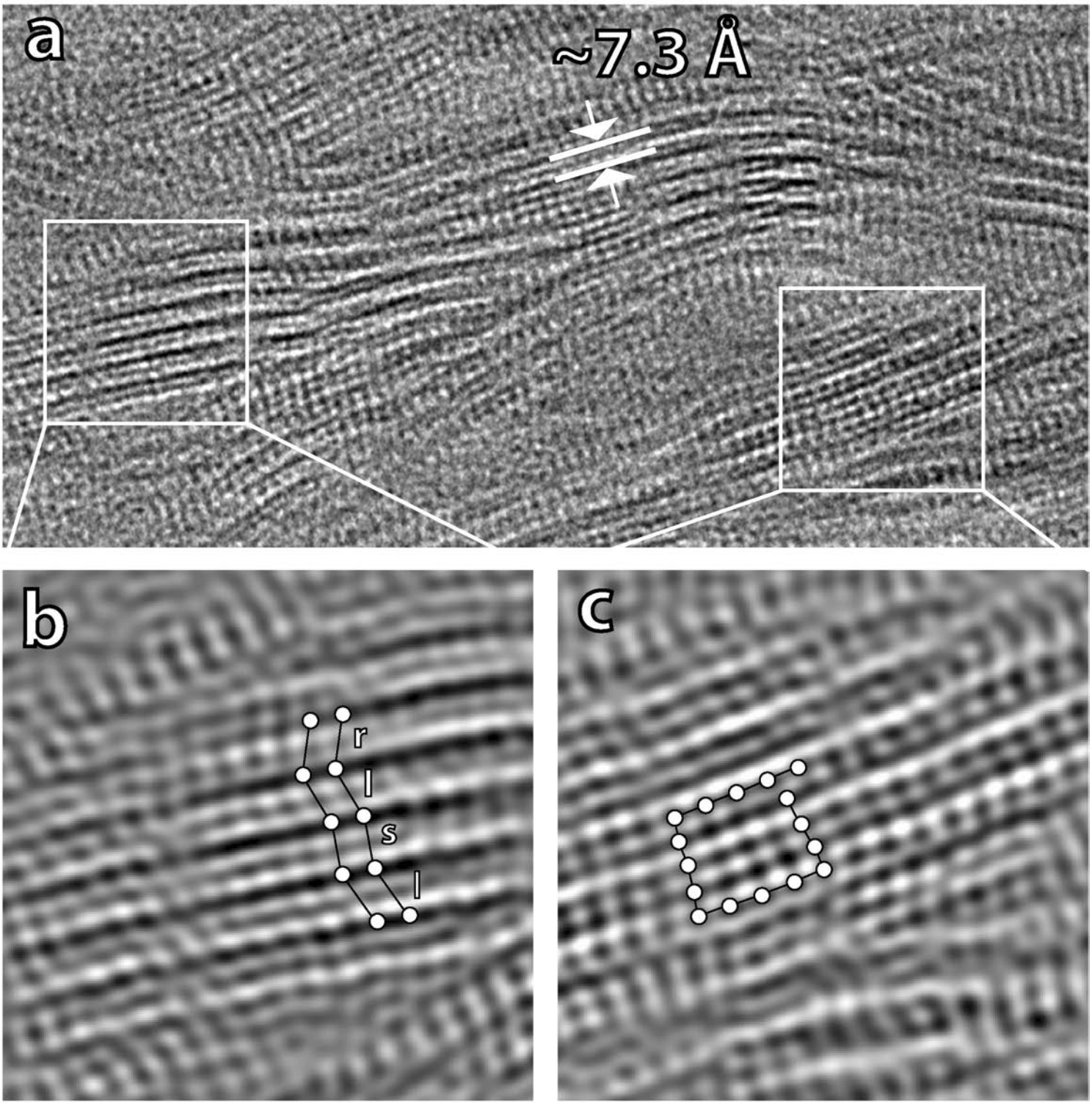

Always consult and cite the final, published document. See http:/www.minsocam.org or GeoscienceWorld

This is a preprint, the final version is subject to change, of the American Mineralogist (MSA)
Cite as Authors (Year) Title. American Mineralogist, in press.
DOI: https://doi.org/10.2138/am-2018-6229

Table 1. EDXRF bulk analyses of the ultramafic host rock.

Wt%	N1	N2	Q268*
MgO	38.31	35.64	39.59
Al_2O_3	2.66	1.75	5.62
SiO_2	35.62	39.60	36.64
SO_3	2.47	3.08	*n.r.*
Cl	0.00	0.03	*n.r.*
K_2O	0.03	0.02	0.25
CaO	1.23	0.60	0.36
TiO_2	0.17	0.08	*traces*
V_2O_5	0.02	0.01	*n.r.*
Cr_2O_3	0.68	0.56	0.46
MnO	0.16	0.16	0.05
FeO	9.34	12.59	10.67
Fe_2O_3	5.02	4.80	4.53
NiO	0.34	0.44	0.19
CuO	0.05	0.05	*n.r.*
ZnO	0.02	0.02	*n.r.*
SnO_2	0.03	0.03	*n.r.*
LOI/H_2O	3.85	0.55	2.13
Sum	100.00	100.00	100.49

*Bertolani (1968); *n.r.* = not reported.

Always consult and cite the final, published document. See http:/www.minsocam.org or GeoscienceWorld

This is a preprint, the final version is subject to change, of the American Mineralogist (MSA)
Cite as Authors (Year) Title. American Mineralogist, in press.
DOI: https://doi.org/10.2138/am-2018-6229

Table 2. WDS-EMP analyses of Ni-serpentine from Campello Monti (averages and ranges) carried out on the intermediate zones (zone 2 in Fig. 5) of three different samples and distinguished according to their backscattered (BSE) contrast (analyses calculated on the basis of 7 oxygens).

	GC1				GC2				GC3	
	BSE bright		BSE dark		BSE bright		BSE dark		bright and dark	
	1	range	2	range	3	range	4	range	5	range
MgO	1.52	1.43 - 1.59	4.85	4.32 - 5.91	1.44	1.10 - 2.08	4.43	4.20 - 4.63	4.39	2.90 - 5.96
Al_2O_3	0.02	0.00 - 0.05	0.02	0.00 - 0.03	0.03	0.00 - 0.06	0.02	0.02 - 0.03	0.02	0.00 - 0.07
SiO_2	33.15	32.93 - 33.51	34.07	33.33 - 34.84	32.34	31.89 - 32.70	33.70	32.88 - 34.22	34.76	32.90 - 35.99
SO_3	0.28	0.00 - 0.51	0.16	0.00 - 0.47	0.60	0.44 - 0.75	0.66	0.38 - 0.96	0.55	0.23 - 1.11
MnO	0.13	0.10 - 0.17	0.04	0.00 - 0.09	0.29	0.09 - 0.52	0.04	0.01 - 0.07	0.06	0.01 - 0.11
FeO	0.01	0.00 - 0.02	0.02	0.01 - 0.03	0.02	0.00 - 0.04	0.01	0.00 - 0.04	0.03	0.00 - 0.08
CoO	0.93	0.87 - 1.00	0.58	0.30 - 0.96	2.32	1.55 - 2.72	1.13	0.82 - 1.70	1.07	0.56 - 1.86
NiO	48.32	45.23 - 49.95	42.80	40.48 - 45.73	51.30	50.75 - 52.16	48.18	46.88 - 49.09	49.41	47.41 - 52.96
CuO	2.55	2.55 - 2.56	2.80	2.61 - 3.03	2.32	2.04 - 2.59	2.47	2.31 - 2.61	2.25	1.29 - 3.42
Total	86.92	83.97 - 88.56	85.33	82.73 - 89.57	90.66	90.06 - 91.60	90.66	89.36 - 91.51	92.54	90.61 - 93.59
Mg	0.144	0.133 - 0.153	0.447	0.406 - 0.525	0.132	0.102 - 0.190	0.395	0.380 - 0.410	0.382	0.258 - 0.509
Al	0.002	0.000 - 0.003	0.001	0.000 - 0.003	0.002	0.000 - 0.004	0.002	0.002 - 0.002	0.002	0.000 - 0.005
Si	2.092	2.063 - 2.125	2.115	2.073 - 2.148	1.997	1.954 - 2.024	2.014	1.995 - 2.028	2.032	1.998 - 2.066
S	0.014	0.000 - 0.025	0.008	0.000 - 0.022	0.028	0.021 - 0.035	0.030	0.017 - 0.044	0.024	0.010 - 0.047
Mn	0.007	0.005 - 0.009	0.002	0.000 - 0.005	0.015	0.005 - 0.027	0.002	0.001 - 0.004	0.003	0.001 - 0.005
Fe	0.000	0.000 - 0.001	0.001	0.001 - 0.001	0.001	0.000 - 0.002	0.001	0.000 - 0.002	0.002	0.000 - 0.004
Co	0.047	0.044 - 0.050	0.029	0.014 - 0.049	0.115	0.076 - 0.135	0.054	0.039 - 0.083	0.050	0.026 - 0.087
Ni	2.452	2.343 - 2.508	2.135	2.074 - 2.189	2.548	2.526 - 2.570	2.316	2.289 - 2.345	2.326	2.169 - 2.537
Cu	0.122	0.120 - 0.124	0.131	0.124 - 0.146	0.108	0.096 - 0.120	0.112	0.103 - 0.120	0.099	0.060 - 0.150
$\Sigma_{T\text{-cat.}}$	2.094	2.066 - 2.125	2.116	2.073 - 2.150	1.999	1.958 - 2.024	2.016	1.997 - 2.030	2.034	1.999 - 2.067
$\Sigma_{O\text{-cat.}}$	2.772	2.676 - 2.822	2.745	2.684 - 2.853	2.919	2.867 - 2.983	2.880	2.854 - 2.909	2.861	2.774 - 2.934

Average composition of 3, 3, 3, 3, and 9 spots for analysis 1, 2, 3, 4, and 5, respectively.

Always consult and cite the final, published document. See http:/www.minsocam.org or GeoscienceWorld

This is a preprint, the final version is subject to change, of the American Mineralogist (MSA)
Cite as Authors (Year) Title. American Mineralogist, in press.
DOI: https://doi.org/10.2138/am-2018-6229

Table 3. WDS-EMP spot analyses referring to Ni-serpentine from the inner and outer zones (zone 1 and 3 of Fig. 5, respectively) and to the most deviating compositions found in the outer zone (analyses calculated on the basis of 7 oxygens).

	Inner zone (1)		Outer zone (3)											
	GC1	GC2	GC1					GC3						
	1	2	3	4	5	6	7	8	9	10	11	12	13	14
MgO	2.56	3.12	7.88	8.56	0.42	0.49	0.60	6.82	10.22	0.48	0.46	4.88	4.69	0.83
Al_2O_3	0.09	0.02	0.06	0.06	10.09	9.79	3.90	0.20	1.76	16.80	17.04	0.00	0.00	4.50
SiO_2	31.80	33.68	37.89	37.37	27.72	27.64	32.88	35.74	40.47	18.65	18.69	35.89	34.59	33.93
SO_3	0.93	1.14	0.13	0.60	1.32	1.72	0.95	0.60	0.47	2.91	3.49	0.72	0.20	0.69
MnO	0.13	0.00	0.10	0.10	0.01	0.03	0.01	0.09	0.00	0.04	0.00	0.11	0.07	0.03
FeO	0.06	0.04	0.02	0.02	1.53	0.09	0.55	0.06	0.12	0.16	0.00	0.07	0.03	2.79
CoO	0.44	0.70	0.83	0.92	0.45	0.29	0.29	1.11	0.73	0.33	0.28	1.14	0.58	0.29
NiO	50.47	50.11	40.35	39.05	31.11	29.23	22.74	44.60	32.76	30.79	30.27	46.68	49.61	24.08
CuO	2.46	3.23	4.28	4.48	17.02	21.78	25.46	3.42	4.59	14.97	14.15	2.68	2.10	19.09
Total	88.95	92.04	91.55	91.16	89.67	91.06	87.40	92.64	91.13	85.14	84.39	92.17	91.86	86.22
Mg	0.237	0.276	0.661	0.717	0.038	0.043	0.055	0.580	0.815	0.045	0.044	0.420	0.412	0.075
Al	0.007	0.001	0.004	0.004	0.715	0.687	0.283	0.013	0.111	1.251	1.263	0.000	0.000	0.323
Si	1.976	1.999	2.132	2.099	1.667	1.647	2.020	2.037	2.165	1.179	1.176	2.071	2.041	2.066
S	0.043	0.051	0.006	0.025	0.059	0.077	0.044	0.025	0.019	0.138	0.165	0.031	0.009	0.031
Mn	0.007	0.000	0.005	0.005	0.001	0.001	0.001	0.004	0.000	0.002	0.000	0.005	0.003	0.002
Fe	0.003	0.002	0.001	0.001	0.077	0.005	0.028	0.003	0.005	0.009	0.000	0.003	0.002	0.142
Co	0.022	0.033	0.037	0.041	0.021	0.014	0.014	0.051	0.031	0.017	0.014	0.053	0.027	0.014
Ni	2.523	2.392	1.827	1.765	1.505	1.401	1.124	2.045	1.409	1.565	1.531	2.167	2.354	1.179
Cu	0.116	0.145	0.182	0.190	0.773	0.980	1.182	0.147	0.186	0.715	0.672	0.117	0.093	0.878
$\Sigma_{T\text{-cat.}}$	1.983	2.000	2.136	2.103	2.382	2.334	2.303	2.050	2.276	2.430	2.438	2.071	2.041	2.389
$\Sigma_{O\text{-cat.}}$	2.908	2.848	2.713	2.719	2.415	2.445	2.404	2.830	2.447	2.353	2.261	2.765	2.892	2.290

1-2: representative analyses of the inner zone; 3-4 and 8-9 representative analyses of the Mg-richest bands; 12-13: representative analyses of Mg-bearing népouite, very similar to those of the BSE dark bands of the intermediate zone (Table 2); 5-6 and 10-11: representative analyses of the Al-richest bands; 7 and 14: representative analyses of the Cu-richest bands.

Always consult and cite the final, published document. See http:/www.minsocam.org or GeoscienceWorld

This is a preprint, the final version is subject to change, of the American Mineralogist (MSA)
Cite as Authors (Year) Title. American Mineralogist, in press.
DOI: https://doi.org/10.2138/am-2018-6229

Table 4. XRPD data and crystallographic parameters of the Ni-serpentine from Campello Monti as compared with pecoraite and népouite from Kwangcheon, Korea (Song et al. 1995).

Ni-Srp Campello Monti						Pecoraite Kwangcheon				Népouite Kwangcheon			
hkl	d_{obs}	d_{calc} [a]	*hkl*	d_{calc} [b]	*I*%	*hkl*	d_{obs}	d_{calc}	*I*%	*hkl*	d_{obs}	d_{calc}	*I*%
002	7.596	7.375	001	7.363	100	002	7.357	7.364	100	001	7.308	7.313	100
110	4.565	4.567	010	4.570	20	110	4.544	4.543	30	100	4.586	4.586	46
004	3.652	3.688	002	3.682	50	004	3.639	3.652	80	002	3.654	3.656	65
130	2.659	2.646	110	2.638	69	200	2.626	2.631	40	110	2.644	2.648	33
006	2.460	2.458	003	2.454	60	202	2.447	2.450	40	111	2.490	2.490	55
116	2.137	2.136	112	2.145	7	060	1.529	1.528	80	112	2.140	2.145	16
151	1.716	1.720	210	1.727	3					113	1.789	1.793	10
060	1.532	1.530	300	1.523	83					210	1.732	1.733	12
261	1.315	1.315	220	1.319	11					300	1.530	1.529	66
										301	1.499	1.496	24
										302	1.410	1.410	11
										220	1.321	1.324	10
										303	1.298	1.295	12
a		5.27(2)		5.28(1)				5.27				5.295	
b		9.18(1)						9.17					
c		14.76(3)		7.36(2)				14.74				7.313	
b		92.16						92.05					
RMs		0.0958		0.1134									

[a]Cell refinement in the *C*2/*m* pecoraite 2M_{c1} structure; [b]cell refinement in the *P*31*m* népouite 1*T* structure.

Always consult and cite the final, published document. See http:/www.minsocam.org or GeoscienceWorld

This is a preprint, the final version is subject to change, of the American Mineralogist (MSA)
Cite as Authors (Year) Title. American Mineralogist, in press.
DOI: https://doi.org/10.2138/am-2018-6229

Table 5. Positions (cm^{-1}) and proposed assignment for peaks observed in the FTIR spectra of the Ni-serpentine from Campello Monti.

Pecoraite [2]	Pecoraite synth.[1]	Nepouite [2]	Nepouite Synth.[3]	This work	Assignment
3683	3650	3685	**3648**	**3646**	Inner surface O-H in-phase stretching
3645	3630	3672	**3610**	**3610**	Inner surface O-H out-of-phase stretching
3529, 3425	3440	3430		3400	Water stretching
3288					Water bending overtone
	1674	1635			Water bending
	1225				Si-O stretch.
			1080	1055	Apical Si-O stretch
1068, 1018, 982, 948	1043, 1005, 900	1040, 1020	984	994	In plane Si-O stretching
839, 820	792				Ni-OH deformation
761					
660, 628	647	**672**	**674**	**673**	Ni-OH libration
607		605	600		$\nu_2(SO_4)$
		536			(Fe-O,OH), lattice modes
		500			(Mg,Ni)-O stretching
	460	465		463	O-Si-O bending
		453	455		Ni-O stretching
	425	427	426, 377, 361	428	O-Si-O bending

[1] Kloprogge et al. (2000); [2] Frost et al. (2008); [3] Baron and Petit (2016). Matching bands in bold to facilitate comparison.

Always consult and cite the final, published document. See http:/www.minsocam.org or GeoscienceWorld